Water Resources Research

RESEARCH ARTICLE
10.1029/2020WR027531

Representing Intercell Lateral Groundwater Flow and Aquifer Pumping in the Community Land Model

Farshid Felfelani[1], David M. Lawrence[2], and Yadu Pokhrel[1]

[1]Department of Civil and Environmental Engineering, Michigan State University, East Lansing, MI, USA, [2]Climate and Global Dynamics Laboratory, National Center for Atmospheric Research, Boulder, CO, USA

Key Points:

- A new prognostic groundwater model is implemented into the latest version of the Community Land Model (CLM5)
- The new model accounts for lateral groundwater flow and conjunctive use of groundwater and surface water for irrigation
- Significant improvements are achieved in simulating the spatiotemporal dynamics of water level over the heavily exploited US aquifers

Supporting Information:

- Supporting Information S1

Correspondence to:
Y. Pokhrel,
ypokhrel@egr.msu.edu

Citation:
Felfelani, F., Lawrence, D. M., & Pokhrel, Y. (2020). Representing intercell lateral groundwater flow and aquifer pumping in the community land model. *Water Resources Research*, *56*, e2020WR027531. https://doi.org/10.1029/2020WR027531

Received 17 MAR 2020
Accepted 22 NOV 2020

Abstract Representation of subsurface hydrology in global land surface models has been advanced but outstanding challenges and opportunities remain, especially in better simulating lateral groundwater flow and aquifer pumping for irrigation. This study improves the representation of groundwater in the latest version of the Community Land Model (version 5) by implementing a prognostic groundwater module that accounts for lateral groundwater flow, aquifer pumping, and conjunctive use of groundwater and surface water for irrigation. In particular, we introduce—for the first time—explicit representation of steady-state well equation in large-scale hydrological modeling. Simulations are conducted at ~5 km resolution over the conterminous US. Groundwater level, terrestrial water storage (TWS), and river discharge are evaluated over the major US aquifers and river basins using in situ observations of groundwater and river discharge and the TWS inferred from the Gravity Recovery and Climate Experiment (GRACE) satellites. The implementation of groundwater pumping results in significant improvements in simulation of spatiotemporal water-level change over the US High Plains and Central Valley Aquifer (CVA) and that of TWS over the CVA. Improvements in river discharge over the major US river basins are also achieved but are not substantial. Furthermore, the representation of pumping leads to certain overestimation in TWS trend compared to GRACE data in regions with high groundwater withdrawals. The consideration of lateral groundwater flow provides improvements in the subsurface response to pumping and natural wet and dry cycles, particularly at the grid cell level. These results provide a basis for improved groundwater modeling over large scales.

1. Introduction

Groundwater supplies ~40% of irrigation and household and ~30% of industrial water use globally (Döll et al., 2012). The generally high-quality water, long residence time, and strong resilience to climate variability (Cuthbert et al., 2019) make groundwater a dependable freshwater resource in many (semi)arid areas, which has led to a rapid increase in groundwater use, especially to sustain rising water demands for increased food production (Pokhrel et al., 2015; Wada et al., 2014). Such groundwater overexploitation has caused an alarming rate of aquifer storage depletion worldwide (Gleeson et al., 2012; Pokhrel et al., 2015; Wada et al., 2010), making groundwater use fundamentally unsustainable that has not only impacted water supplies, but also gravely altered natural hydrologic regimes and deteriorated ecosystem health (Gleeson et al., 2012; Siebert et al., 2010).

Hydrologically, groundwater acts as a buffer that directly modulates soil moisture and is coupled to surface water through a relatively slow, two-way water exchange; groundwater converges to streams and lakes as baseflow and recharges naturally by water percolating down from the surface (de Graaf et al., 2015, 2017; Fan et al., 2007, 2019; Zeng et al., 2018). Additionally, groundwater is tightly linked with other hydrological processes, such as surface energy balance and land-atmosphere interactions (e.g., through evapotranspiration and precipitation) in critical zones where water table is shallow (Condon & Maxwell, 2019; Kollet & Maxwell, 2008). It has been shown that in relatively humid regions water table depth is a major determinant of water and energy exchange between groundwater, land surface, and atmosphere (Gleeson et al., 2011). Other studies have also shown that the use of groundwater for irrigation can have implications on regional-to-global climate and weather systems (Devanand et al., 2019; Yamada & Pokhrel, 2019). Therefore, the overexploitation of groundwater and the resulting storage depletion caused by increasing human land-water management activities (e.g., land use change, irrigation, and pumping) has important implications on a

range of groundwater-dependent hydrologic systems including rivers, lakes, and wetlands across the globe (de Graaf et al., 2019; Wada et al., 2010).

Benefiting from ground observations and satellite data including terrestrial water storage (TWS) inferred from the Gravity Recovery and Climate Experiment (GRACE) satellite mission, our ability to understand and monitor the changes in global groundwater systems have been unprecedentedly advanced (Döll, Müller Schmied, et al., 2014; Felfelani et al., 2017; Gleeson et al., 2012; Rodell et al., 2009, 2018; Scanlon, Longuevergne, et al., 2012). Concurrently, the modeling community has put concerted efforts to better simulate groundwater dynamics and characterize the connections between groundwater and hydrologic fluxes under natural and human-induced drivers (Felfelani, 2019). As a result, there has been a substantial increase in the number of hydrological models that include groundwater representation across scales—local, regional, and global.

While some form of groundwater has been introduced into many land models, the level of complexity in groundwater parameterizations varies widely, operating at varying spatial scales because of constraints posed by data availability and computational costs (Koirala et al., 2019). In a number of regional and global land surface models (LSMs), groundwater is represented as an unconfined aquifer unit, however in a rather simplified manner. Models in this category include the Variable Infiltration Capacity (VIC; Liang et al., 2003), Community Land Model (CLM; Lawrence et al., 2011; Leng et al., 2013; Oleson et al., 2013; Zeng et al., 2018), the upgraded version of the MATSIRO (i.e., HiGW-MAT; Pokhrel et al., 2012, 2015, 2017), MIROC-INTEG (Yokohata et al., 2020), and Noah-Multiparameterization model (Noah-MP; Nie et al., 2018; Niu et al., 2011).

Models developed for relatively smaller scales (e.g., local to regional) include relatively sophisticated groundwater representation (e.g., coupled three-dimensional groundwater flow and solute transport). For example, the US Geological Survey (USGS) regional MODFLOW model simulates the three-dimensional steady-state and transient groundwater flow based on a rectangular structured finite-difference grid (Panday et al., 2013) and, more recently, unstructured grids (Feinstein et al., 2016). MODFLOW only simulates the subsurface hydrology and needs to be either forced by recharge rates and water levels in surface water bodies or coupled with an LSM or a global hydrological model (GHM) (de Graaf et al., 2015). ParFlow (Condon & Maxwell, 2015, 2019; Maxwell & Condon, 2016; Maxwell & Miller, 2005) is a comprehensive and integrated coupled surface water-groundwater model which solves the three-dimensional Richards equation (Richards, 1931) to account for variably saturated soil with very high resolution (e.g., 1 km), however high computation costs make long-term (e.g., multidecadal) simulations over large domains (i.e., continental to global) infeasible with currently available computational resources. LEAF-Hydro-Flood (Fan et al., 2007; Miguez-Macho et al., 2007) is a land hydrology model with a prognostic groundwater scheme that simulates lateral flow and water table dynamics and is used over regional (Chaudhari et al., 2019; Pokhrel et al., 2013) to continental (Shin et al., 2019) scales.

Given the growing interest of the hydrologic community on hyperresolution modeling over large domains (Bierkens et al., 2015), it is imperative to improve groundwater representation in large-scale models to more realistically simulate climate-human-groundwater interactions (Pokhrel et al., 2016). Among large-scale models, GHMs (e.g., WaterGAP, PCR-GLOBWB; de Graaf et al., 2015; Döll, Fritsche, et al., 2014; Döll, Müller Schmied, et al., 2014; Wada et al., 2017) employ the middle-of-the-road representation for groundwater and include a relatively comprehensive representation of the impacts of human activities such as groundwater pumping. However, GHMs are designed for offline simulations and not coupled with Earth system models (ESMs). Conversely, LSMs are developed for use within ESM frameworks for both land-only and coupled land-atmosphere simulations, but the majority of LSMs (e.g., CLM, HiGW-MAT, Noah-MP) include simple groundwater schemes that resolve only one-dimensional (vertical) soil moisture-groundwater movement without accounting for lateral groundwater flow. The lateral groundwater flow contribution to the water budget depends on multiple factors such as climate, topography, aquifer properties, and pumping (Feddes et al., 1988; Krakauer et al., 2014; Sophocleous, 2002). Lateral flow is suggested to be insignificant in coarse grid sizes in the order of 0.5°–1° or lower resolutions (Krakauer et al., 2014; Pokhrel et al., 2015) and therefore is generally ignored in global simulations. An additional barrier to the inclusion of lateral flow in large-scale LSMs has been the lack of global hydrological datasets of permeability and depth-to-bedrock, but recent efforts have resulted in potentially useful datasets (Gleeson et al., 2014; Huscroft et al., 2018;

Pelletier et al., 2016; Xie et al., 2018), even though with certain limitations (e.g., low vertical and horizontal resolutions, inconsistencies over state borders, inherent biases). As such, the significant advances in global datasets and computational capabilities have provided new opportunities in higher-resolution hydrological modeling (Bierkens et al., 2015), including the representation of intercell lateral groundwater flow in LSMs.

Lateral groundwater flow was first parametrized based on Darcy's law in a regional hydrological model, the LEAF-Hydro (Fan et al., 2007). A handful of studies since then have adopted the approach to account for intercell lateral flow mostly for regional to continental scales at high spatial resolution (i.e., ~1–5 km) (Xie et al., 2018; Zeng et al., 2016, 2018). In a recent study, intrahillslope lateral flow was introduced into CLM to capture the impact of lateral flow across representative hillslopes within a grid cell at the hillslope scales (Swenson et al., 2019), thereby enabling research on coupled hillslope-hydrology-vegetation interactions (Chaney et al., 2018; Fan et al., 2019). This representation of within grid-cell (as opposed to intercell) lateral flow is highly relevant for continental to global studies using coarse resolutions (i.e., >0.5°), at which the representation of intercell lateral flow is not generally meaningful (Krakauer et al., 2014).

Furthermore, to better replicate irrigation practices where groundwater storage supplies irrigation in conjunction with surface water, groundwater needs to be linked with irrigation through pumping. However, pumping is missing in many models (e.g., LEAF-Hydro, CLM) and relatively simplistically quantified (e.g., lateral flow not represented, groundwater assumed to be the sole source of irrigation) in some models, for example, HiGW-MAT (Pokhrel et al., 2015), CLM (Leng et al., 2014), and Noah-MP (Nie et al., 2018). Some of the models equipped with a pumping scheme have been reported to suffer from systematic biases in groundwater related fluxes and states (e.g., overestimation of groundwater storage loss caused by pumping; Nie et al., 2018; Pokhrel et al., 2015). Additionally, the absence of lateral flow generally leads to underrepresentation of the direct impact of groundwater withdrawals on surrounding areas (Pokhrel et al., 2015).

The goal of this study is to address some of the aforementioned gaps and limitations in groundwater modeling in global LSMs through the representation of intercell lateral groundwater flow and aquifer pumping, implemented in the codebase of the latest version of the CLM (version 5; CLM5). The new version of the model explicitly simulates groundwater pumping, accounts for conjunctive use of groundwater and surface water for irrigation, and represents lateral flow based on two approaches: (1) the conventional Darcy's law for natural recharge- and topography-driven lateral flow and (2) the steady-state well equation for pumping-induced lateral flow. To the authors' best knowledge, this study is the first to represent the steady-state well equation in large-scale hydrological models. The specific objectives are to: (1) evaluate the improvements achieved in the simulation of groundwater, TWS, and river discharge using the new prognostic groundwater scheme across the conterminous US (CONUS); (2) investigate the effects of groundwater withdrawal on water table change across the heavily exploited US aquifers; and (3) explore the role of lateral flow in subsurface hydrology both in the natural condition and under the impact of pumping.

2. Data and Methods

2.1. Data

To specify the contribution of groundwater and surface water to total irrigation water withdrawals in the model, we use the county-level census data of irrigation water withdrawals (averaged for 1985–2015) from the USGS (Figure S1), available at 5-year interval since 1985 (Dieter et al., 2018; Maupin et al., 2014). Fractional groundwater contribution varies significantly ranging from zero in most of the counties in the Colorado Plateau, to around 40% in the Central Valley Aquifer (CVA) and the Snake River Plain to over 90% in most counties in the High Plains Aquifer (HPA) and Mississippi Alluvial Plain (Figure S1). The county-level USGS data are also used to validate the simulated irrigation water requirement and groundwater-supplied irrigation withdrawals.

The equilibrium water table depth (i.e., climatologic mean that represents the long-term balance between the climate-driven recharge and the topography-driven lateral flow) (Fan et al., 2013), aggregated to 0.25° resolution, is used to initialize the water table depth in CLM5 to reduce the spin-up period (Zeng et al., 2018). To validate the simulated water-level change across the selected regions (i.e., regions with high depletion rate) within the HPA, we use the USGS winter time water-level data from monitoring wells (McGuire, 2014,

2017). The USGS observational wells are filtered considering the length of records and the long-term mean water table depth. Wells within a given region of interest are selected if (1) there is at least 10 years of data available and (2) the mean water table depth is within 5 m of 75th percentile of long-term water-level mean of all wells in that region. Using this filtering approach, 366 wells in southern Nebraska (NE_S), 31 wells in southwest of Nebraska (NE_SW), 32 wells in southwest of Kansas (KS_SW), 23 wells in north-center of Texas (TX_NC), 14 wells in northeast of Nebraska (NE_NE), and 9 wells in northwest of Nebraska (NE_NW) are selected. The USGS river discharge data are used to validate the seasonal streamflow at the selected gauging stations across major river basins within the CONUS.

To validate the decadal TWS trends from CLM5 simulations, we use five monthly GRACE products: two mass concentration (mascon) solutions from the Center for Space Research (CSR; Save et al., 2016) at University of Texas at Austin and Jet Propulsion Laboratory (JPL; Watkins et al., 2015; Wiese, Yuan, et al., 2016) at California Institute of Technology, and three spherical harmonic (SH) products from CSR, JPL, and the German Research Center for Geoscience (GFZ). While the CSR mascons are directly used at the resolution of 0.5° × 0.5°, scaling coefficients are applied to the JPL mascons to downscale the data from the native 3° × 3° resolution to the 0.5° × 0.5° grids by redistributing the mass within each mascon (Nie et al., 2018, 2019; Wiese, Landerer, et al., 2016). The level-3 SH solutions are provided at 1° × 1° grid resolution (available for download at https://podaac.jpl.nasa.gov/GRACE). The mascon solutions have been shown to be less affected by the leakage error, less dependent on using the scaling factors, and require less postprocessing (e.g., destriping filtering is not required for mascon products) than the SH solutions (Long et al., 2015; Scanlon et al., 2016; Watkins et al., 2015). Here, we use all five products to increase the robustness of the comparison and highlight the uncertainties among different GRACE products. Trend values are calculated for GRACR products and simulations based on the least squares regression and Theil-Sen slope estimator. The significance of trend values are evaluated using the Wald test (Gouriéroux et al., 1982) and the nonparametric Mann-Kendall trend test (Kendall, 1975; Mann, 1945) at the 5% significance level. Furthermore, we quantify the pumping-induced TWS change over the major US aquifers by deducting the TWS trend of the simulation with lateral flow from that of the simulation with lateral flow and pumping.

2.2. The CLM5

CLM5 is the land component of the Community Earth System Model version 2 (Danabasoglu et al., 2020). It includes a comprehensive set of underlying physical processes and parametrizations in hydrology (e.g., hydrology of canopy, soil, groundwater, snow, and river flow), surface energy fluxes, and biogeochemical cycling (e.g., photosynthesis and phenology, carbon and nitrogen cycles, methane production) (Lawrence et al., 2019). CLM5 includes a crop model, a soil-moisture-deficit-based irrigation scheme, and other agricultural management practices (Lawrence et al., 2019). In the standard CLM5, the irrigation water requirement is applied to the soil column as add-on to precipitation (at 6 a.m. local time), withdrawing water from surface water (i.e., water in the main channel in the river routing scheme). Where water in river channels is not sufficient to meet irrigation demands, the deficit is supplied by a virtual source (e.g., ocean model) or if irrigation limitation is set, irrigation amount is restricted to that available within the main river channel in the grid cell.

The subsurface is represented using a high vertical resolution and improved solution to the Richard's equation to resolve soil water movement across layers. CLM5 allows users to select among multiple configurations or parametrizations for a number of processes, enabling users and model developers to choose the parameterizations that best address their objectives. For example, users can select between a head-based and a zero flux lower boundary condition for the soil column. If the unconfined aquifer beneath the soil column is activated, the drainage from the lowest soil layer (recharge; q_{rech}) is controlled by a head-based lower boundary condition (i.e., $q_{\mathrm{rech}} = q_i + \frac{\partial q_i}{\partial \theta_{\mathrm{liq},i}} \partial \theta_{\mathrm{liq},i}$; where q_i is the water flux across the lowest interface and $\theta_{\mathrm{liq},i}$ is the liquid volumetric soil moisture). When the water table is within the soil column, recharge rate is diagnosed using Darcy's equation across the water table. Soil thickness is constant (8.5 m) globally and water table depth can vary from 0 to 80 m. In this configuration, subsurface runoff decays exponentially depending on the water table depth (z_{wt}), that is, $q_{\mathrm{sub}} = \Theta_{\mathrm{ice}} q_{\mathrm{drai,max}} \exp\left(-f_{\mathrm{drai}} z_{wt}\right)$, where Θ_{ice} is the ice

impedance factor, $q_{\mathrm{drai,max}}$ is the maximum subsurface runoff when $z_{wt} = 0$ and is set to $q_{\mathrm{drai,max}} = 10\sin(\beta)$ to best compare with observations in global simulations, β is the mean grid cell topographic slope in radians, and f_{drai} is the decay factor (Niu et al., 2005). This groundwater parameterization was initially introduced in CLM4.5 and is retained as an option in CLM5.

The default version of CLM5 includes a new subsurface hydrology scheme in which the bulk aquifer layer below the model soil column is removed and the head-based lower-boundary condition is replaced by a zero-flux boundary condition at the base of the soil column. Additionally, soil thickness (depth-to-bedrock) is spatially explicit (depths between 0.4 and 8.5 m are allowed, with the 8.5-m depth chosen to allow for relatively deep soil water stores for use, for example, by tropical trees, but shallow enough to maintain reasonably short spin-up time). This scheme results in improved simulation of TWS seasonal and interannual variability (Swenson & Lawrence, 2015). The water table is determined by identifying the first soil layer above the bedrock with soil water saturation fraction of less than 0.9. A drawback of this groundwater configuration is that the water table depth is only resolved when saturated soil layers exist within the active soil portion of the ground column (i.e., max 8.5 m in default CLM5). Deeper water table positions, as is common in arid or semiarid regions, are not resolved and are set to 8.5 m. Finally, surface and subsurface runoff is routed across the landscape using the process-based Model for Scale Adaptative River Transport (MOSART, Li et al., 2013), which simulates the surface water dynamics (i.e., streamflow, channel velocity, and water depth) based on kinematic wave formulations (Lawrence et al., 2019).

2.3. Representation of Pumping in CLM5

To consider conjunctive water use for irrigation, the surface water-supplied fraction (i.e., determined by the USGS data) of the irrigation water requirement is withdrawn from the main channel in MOSART (if adequate water is available). The rest of the irrigation water is then extracted from the aquifer layer if water table is below the soil column (or from soil layers when water table is within the soil column). Here, we incorporate a groundwater pumping scheme into CLM5, in which water is withdrawn to satisfy the groundwater-supplied portion of the irrigation requirement in a grid cell. The water balance of a grid cell with pumping (Pokhrel et al., 2015) is expressed as:

$$\frac{dS_g}{dt} = AR - GW_{pr} - Q_r \tag{1}$$

where dS_g / dt is the groundwater storage change, R is the net recharge (i.e., the flux between the unsaturated soil and the groundwater), $A = \Delta x \Delta y$ is the grid cell area, and Q_r is the groundwater discharge to the river. GW_{pr} is the groundwater pumpage rate, which is extracted from the aquifer layer (when water table is below the soil column) or soil layers (when water table is within the soil column) in sequential order starting from the soil layer right below the water table. Any GW_{pt} residual not satisfied by the amount of water taken from the soil layers is taken from the underlying aquifer layer. The water table depth is then lowered as:

$$z_{wt}^{'} = z_{wt} + \frac{dGW_{pr}}{S_y} \tag{2}$$

where $z_{wt}^{'}$ and z_{wt} are the updated and old water table depths, respectively, dGW_{pr} is the portion of total groundwater pumpage extracted from a soil layer, and S_y is the specific yield of the aquifer, diagnosed in CLM5 based on the soil properties and water table location. Finally, the liquid water storage of the soil layers and the aquifer layer are also updated based on the water extracted for pumping.

2.4. Lateral Groundwater Flow Using Darcy's Law

The lateral groundwater flow in cells with no pumping ($GW_{pr} = 0$) is represented by Darcy's law following Fan et al. (2007). In this approach, the lateral flow is included in the groundwater mass balance for a grid cell by generalizing Equation 1 as:

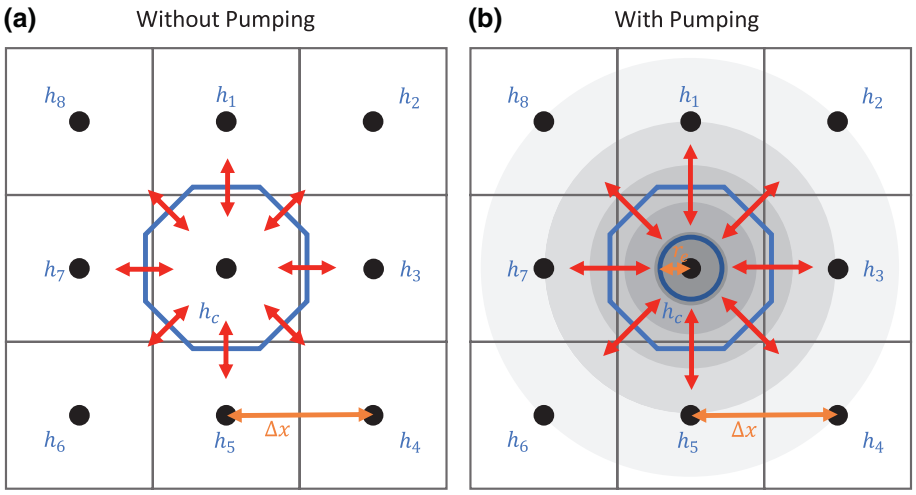

Figure 1. Schematic of lateral groundwater flow between a grid cell and the eight neighboring cells in the absence (a) and existence (b) of pumping. Note that the entire groundwater-supplied irrigation water requirement of a grid cell is assumed to be withdrawn from a single well (with the radius of r_e).

$$\frac{dS_g}{dt} = AR + \sum_{1}^{8} Q_n - Q_r \tag{3}$$

where $\sum_{1}^{8} Q_n$ is the net lateral flow between the center cell and its neighboring cells and $Q_r$is the groundwater discharge to rivers, which can be dropped for a nonriver cell. When the water table is below the soil column, the net lateral flow is added (removed) to (from) the aquifer storage. If the water table is within the soil column, the positive net lateral flow is added to soil layers in sequential order starting from the soil layer right above the water table and the negative net lateral flow is extracted from soil layers in sequential order starting from the soil layer right below the water table (any residual would be taken from the underlying aquifer layer). The lateral flow is mainly driven by groundwater head difference—induced by climate, topography (i.e., topographic slope in baseflow generation), pumping, and so on—between two cells and computed based on Darcy's law as:

$$Q_n = wT\left(\frac{h_n - h_c}{l}\right) \tag{4}$$

where h_n and h_c are the hydraulic head in nth neighbor and center grid cells, respectively, T is the transmissivity, l is the distance between cells, and $w = \Delta x\sqrt{0.5\tan(\pi / 8)}$ is the width of an imaginary octagon (Figure 1) that replaces the square grid cell to provide an equal chance for all eight sides/neighbors to flow to/from the central cell. Figure 1 shows the schematic diagram of intercell lateral flow in the absence of pumping wells (Figure 1a) and immediate vicinity of a cell with pumping wells (Figure 1b).

The prognostic aquifer transmissivity (T) is also calculated based on the water table depth and hydraulic conductivity for two different cases (Fan et al., 2007). If water table depth is within the model soil column, T=T_1 + T_2, where T_1 is the transmissivity of saturated portion of the soil column (i.e., from the water table to the bottom-most layer) and T_2 is the transmissivity for the depth below the bottom-most layer.

$$T_1 = \begin{cases} \sum_{i=iwt+1}^{n} \left(K_i + \Delta z_i\right) + K_{iwt} \times \left(Z_{h,iwt} - Z_{wt}\right) & \text{for layer } i < n \\ K_n \times \left(Z_{h,n} - Z_{wt}\right) & \text{for layer } n \end{cases} \tag{5}$$

$$T_2 = \int_0^{\infty} K(z')dz' = \int_0^{\infty} K_n \exp\left(-\frac{z'}{f}\right)dz' = K_n \times f \tag{6}$$

where *iwt* is the index of soil layer that includes the groundwater table, K_i is the hydraulic conductivity of layer i, Δz_i is the thickness of soil layer i, $Z_{h,iwt}$ is the bottom interface depth of layer i, Z_{wt} is the groundwater table depth, and n is the total number of soil layers. The aquifer transmissivity for the depth lower than the model soil column (T_2) is estimated using the hydraulic conductivity of the bottom-most layer, exponentially decayed with depth $\left(K = K_n \exp\left(-\frac{z'}{f}\right)\right)$. Here, f is the e-folding length representing the complexity of sediment-bedrock profile (Zeng et al., 2016) and is calculated following the hyperbolic equation presented in Fan et al. (2007) as:

$$f = \frac{a}{1 + b\beta} \text{ for } \beta \le 0.16, \text{and } f = 5\text{m for } \beta > 0.16 \tag{7}$$

where a and b are parameters set to 120 and 150 m, respectively, and β is the terrain slope.

If the water table is below the soil column, the transmissivity is calculated using Equation 6 but for the lower bound equal to the distance from the water table depth and the bottom interface depth of layer n (i.e., $Z_{h,n}$) as:

$$T = \int_{Z_{wt}-Z_{h,n}}^{\infty} K(z')dz' = \int_{Z_{wt}-Z_{h,n}}^{\infty} K_n \exp\left(-\frac{z'}{f}\right)dz' = K_n f \exp\left(\frac{z_{h,n} - z_{wt}}{f}\right) \tag{8}$$

Note that the hydraulic conductivity in the above equations is the lateral hydraulic conductivity determined from the vertical hydraulic conductivity—resolved in the vertical one-dimensional soil movement—and percent of clay in the soil layer as the representative of anisotropy factor $\left(\text{i.e., } C_{\text{clay}} = \frac{K_{\text{lat}}}{K_{\text{ver}}}\right)$ (Fan et al., 2007; Zeng et al., 2016).

2.5. Lateral Groundwater Flow Using Steady-State Well Equation

In finite difference models, a point sink/source of water (e.g., pumping wells) is represented by the grid cell that contains the sink/source. Since the gird cell has dimensions typically much larger than a well diameter and irrigation water is extracted from the entire cell (Section 2.3), the simulated head in a pumping cell does not represent the relatively large head gradient caused by pumping (Anderson et al., 2015). However, it can be reasonably assumed that the simulated head in a pumping cell represents the head at certain distance (r_e) from the center of the cell. Therefore, we consider a virtual single well at the center of pumping cells and compute the lateral flow using the steady-state well equation applied between $r = r_e$ and the center of a neighbor cell following Anderson et al. (2015).

The 2-D form of the groundwater equation with the assumption of lateral isotropy can be written in both the Cartesian (Equation 9) and radial (Equation 10) coordinate systems as:

$$S_y \frac{\partial h}{\partial t} = \frac{\partial}{\partial x}\left(T\frac{\partial h}{\partial x}\right) + \frac{\partial}{\partial y}\left(T\frac{\partial h}{\partial y}\right) + \varepsilon \tag{9}$$

$$S_y \frac{\partial h}{\partial t} = \frac{1}{r}\frac{\partial}{\partial r} Tr \frac{\partial h}{\partial r} + \varepsilon \tag{10}$$

where S_y is the aquifer specific yield, h is the hydraulic head, T is the transmissivity, and ε is the sink/source term. The analytical solution of the radial partial differential equation (Equation 10) for the steady state

condition considering pumping in the boundary condition at well radius (i.e., $r = r_0$, $Q = K\frac{\partial h}{\partial r} \times 2\pi r_0 h$, where Q is the pumping rate $\left[\frac{L^3}{T}\right]$) is given as:

$$\left(\frac{1}{2r}\left(\frac{Q}{\pi} + \varepsilon r_0^2\right) - \frac{\varepsilon r}{2}\right)dr = Tdh \tag{11}$$

Assuming that the head change due to pumping is negligible compared to the aquifer thickness and evaluating the above integral, the solution to Equation 11 can be written as Equation 12, which can be simplified to Equation 13—generally known also as the well equation—assuming a known head (i.e., $r = R, h = H$).

$$\left(\frac{Q}{2\pi} + \frac{\varepsilon r_0^2}{2}\right)\ln r - \frac{\varepsilon r^2}{4} = Th + C \tag{12}$$

$$\left(\frac{Q}{2\pi T} + \frac{\varepsilon; r_0^2}{2T}\right)\ln\frac{R}{r} - \frac{\varepsilon\left(R^2 - r^2\right)}{4T} = H - h \tag{13}$$

The total water pumped in the center cell is supplied by the lateral flow from the eight neighboring cells (Figure 1b) (Anderson et al., 2015). Thus, the lateral flow can be estimated by solving Equation 13 for Q, applying it between the effective well block radius $r = r_e$ and the center of a neighbor cell (i.e., $r = a = \Delta x$ or $\Delta x\sqrt{2}$), which yields:

$$Q_{\text{lat}} = \frac{Q}{8} = \frac{\pi T\left(z_{wt@r_e} - z_{wt@a}\right)}{4\ln\left(\frac{a}{r_e}\right)} + \frac{\varepsilon\pi\left(a^2 - r_e^2\right)}{16\ln\left(\frac{a}{r_e}\right)} - \frac{\pi\varepsilon r_0^2}{8} \tag{14}$$

where $z_{wt@re}$ and $z_{wt@a}$ are the water table depths at $r = r_e$ and $r = a$. Following Anderson et al. (2015), the effective well block radius for the 8-neighbor case is calculated as $r_e = 0.178\Delta x$ (Figure 1b). Note that if recharge is explicitly resolved and directly added to groundwater storage, the recharge terms in Equation 14 should be ignored.

2.6. Experimental Settings

To investigate the separate roles of lateral groundwater flow and pumping, we conduct four sets (i.e., all possible combinations by turning lateral flow and pumping on and off) of CLM5 offline simulations over the CONUS domain at 3 arc-min (~5 km) resolution and forced by the North America Land Data Assimilation System phase II meteorological data. Surface and subsurface runoff is routed using MOSART at 0.125° (~13 km) resolution as in the default CLM5. Table 1 illustrates the groundwater and subsurface configurations for all simulations. Given that the primary objective of this study is to improve the simulation of water table dynamics and better capture the impact of extensive groundwater pumping, we select the active aquifer layer and the head-based recharge (Section 2.2) for implementing lateral flow and pumping.

In the control experiment (CTRL), the aquifer beneath the soil column is activated as in the standard CLM4.5 configuration, which is retained as an option in CLM5.0 (Section 2.2). The CTRL_PumpNoLat is based on CTRL, but groundwater pumping (Section 2.3) for conjunctive use of groundwater and surface water for irrigation is additionally considered. The DarcyLat_NoPump includes lateral flow (Section 2.4) based on Darcy's law (Fan et al., 2007) incorporated into CLM5 considering the same subsurface configuration as in CTRL (i.e., the same lower boundary condition, the same subsurface runoff parameterization, and activated aquifer layer). See Text S1 in the supporting information for the parallel computing architecture and the modifications required for intercell communications due to the implementation of lateral flow. The fourth experiment (DarcyWellLat_Pump) is designed to account for groundwater pumping (Section 2.3) as

Table 1
Experiments and Model Configuration

Simulation	Lower BC	Aquifer layer	Subsurface runoff	Pumping	Soil configuration	Lateral flow
CTRL	Head-based	Active	Exponential	No	20 layers, 8.5 m	No
CTRL_PumpNoLat	Head-based	Active	Exponential	Yes	20 layers, 8.5 m	No
DarcyLat_NoPump	Head-based	Active	Exponential	No	20 layers, 8.5 m	Darcy
DarcyWellLat_Pump	Head-based	Active	Exponential	Yes	20 layers, 8.5 m	Darcy and well equation

Abbreviation: CTRL, control experiment.

well as the lateral flow based on combination of Darcy's law and the steady-state well equation (Section 2.5). That is, in calculating the lateral flow between two grid cells, in case at least one of them is pumping cell (i.e., cell with nonzero groundwater-supplied irrigation demand) Equation 14 applies, and if both are non-pumping cells, Equation 4 applies. This simulation, likewise, uses the same soil configuration and lower boundary condition as in CTRL.

For model spin-up, water table depth is initialized with the equilibrium water table depth from Fan et al. (2013). The CTRL and DarcyLat_NoPump experiments are first spun up for 120 years cyclically using the available atmospheric forcing data. Next, 3 years of recursive simulations are conducted using the forcing data for year 2000 to get the model stabilized for year 2000. Simulations for 2000–2016 period are then conducted. The CTRL_PumpNoLat and DarcyWellLat_Pump simulations are started from CTRL and DarcyLat_NoPump (i.e., spun up for 120 years), respectively, with an extra spin-up of 10 years in transient mode (i.e., with pumping) to avoid these simulations starting with initial condition as in the simulations with no pumping, especially over the highly exploited aquifers. Then, the actual simulation is conducted for 2000–2016 period. Ideally, the transient simulation could be started from the beginning of irrigation development (e.g., 1950 for the HPA) to better replicate the absolute depletion caused by pumping since the predevelopment. However, we chose to conduct a 10-year spin-up in transient mode because our goal is to evaluate the improvements in groundwater simulations resulting from the incorporation of lateral flow and pumping, rather than capture the long-term depletion caused by pumping.

3. Results and Discussion

3.1. Spatial Variability of Groundwater Table Depth

Figure 2 shows the average groundwater table depth for 2000–2016 period from the two control simulations (Figures 2a and 2b) and the differences between DarcyLat_NoPump and CTRL as well as DarcyWellLat_Pump and CTRL_PumpNoLat (Figures 2c and 2d). The water table dynamics and cumulative change are validated next (Section 3.2). In general, water table depth is controlled by the balance between the vertical (recharge from the soil column to the aquifer and capillary flux) and lateral (base flow and lateral groundwater flow) water fluxes (Fan et al., 2007; Swenson & Lawrence, 2015). In the CTRL simulation (Figure 2a), the spatial distribution of groundwater table depth mostly reflects climate patterns in the absence of pumping. That is, across the eastern US with abundant precipitation that contributes largely to aquifer recharge, water table resides within shallow depths (i.e., maximum 8 m from the land surface). Conversely, over the western and southwestern US, water table depth is much deeper (i.e., up to 80 m) owing to less recharge (i.e., in mostly arid and semi-arid climate), steep terrain, and rugged topography (represented by the slope term in the subsurface runoff parameterization). In terms of the water table type and the regional characteristic of groundwater systems (Gleeson et al., 2011), the larger depth and high spatial variabilities over the West and Southwest suggest a recharge-controlled type of groundwater, whereas, shallow water table together with low spatial variability across the Midwest and East suggest a topography-controlled type of groundwater, consistent with Gleeson et al. (2011). The long-term average water table depth in CTRL (Figure 2a) and CTRL_PumpNoLat (Figure 2b) is generally similar in most regions except over highly managed aquifer systems (insets in Figures 2a and 2b) where a large water level drop is caused by pumping. For example, in the HPA water level drops by ~2–10 m in the northern part, ~7–19 m in the central part, and ~10–27 m in the southern part, which are all intensively irrigated using groundwater. Similar patterns can

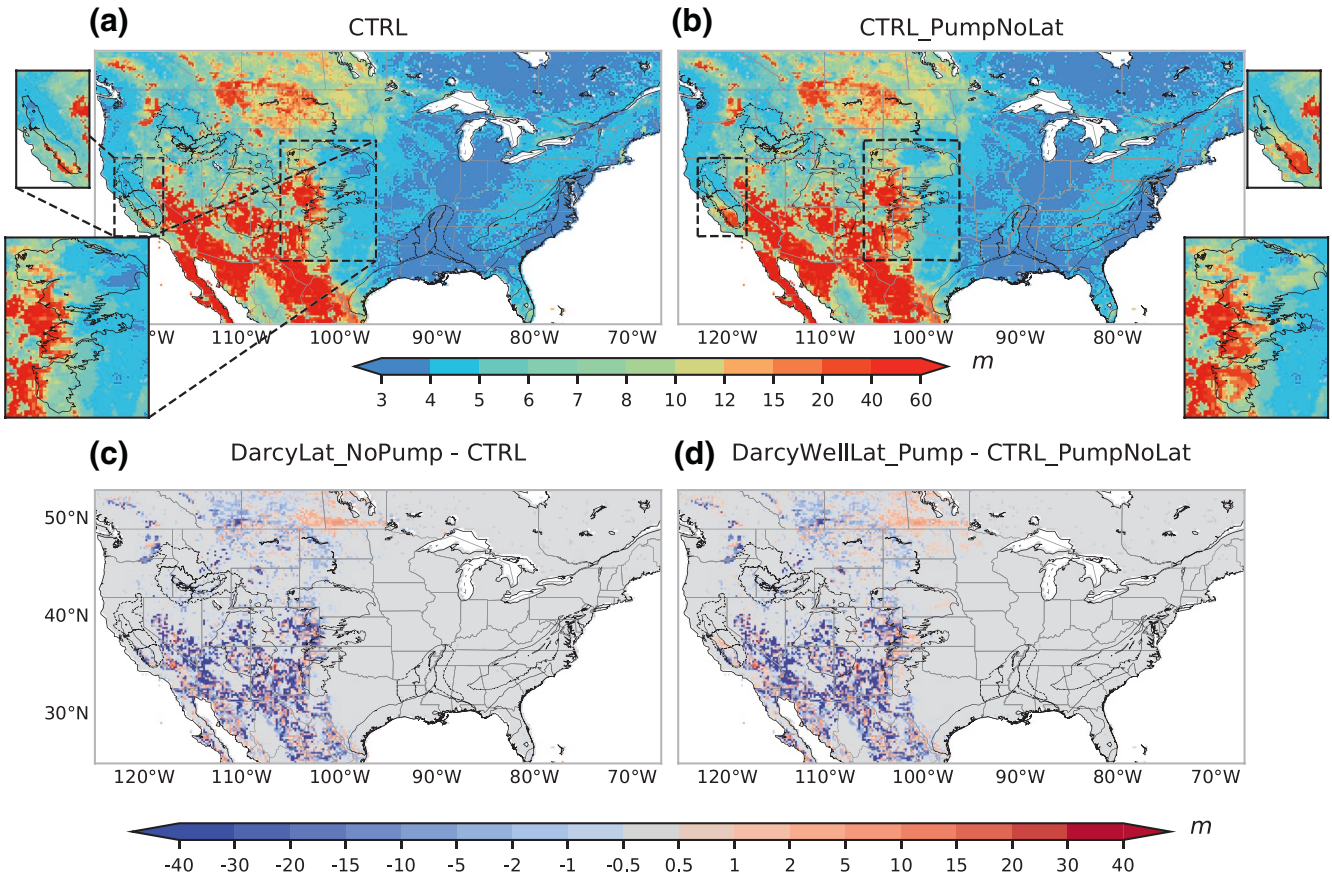

Figure 2. Long-term average water table depth (m) from CTRL and CTRL_PumpNoLat (a and b) and the differences between DarcyLat_NoPump and DarcyWellLat_Pump against CTRL and CTRL_PumpNoLat (c and d), respectively, for 2000–2016. The major US aquifers (i.e., HPA, CVA, Mississippi Alluvial Plain, Snake River Plain, Colorado Plateau, Coastal Lowlands, Piedmont Blue Ridge, and Surficial) are outlined with black color (see Figure S1 for aquifers location). CTRL, control experiment; CVA, Central Valley Aquifer; HPA, High Plains Aquifer.

be seen in the southern part of the CVA (i.e., the San Joaquin River basin) and Snake River Plain where water table drawdown of up to ~17 m and 10 m stands out, respectively. Note that the absolute magnitude of depletion due to irrigation could have potentially been underestimated over regions such as the HPA because of the substantially longer irrigation development period compared to the 10-year spin-up in transient mode considered in this study.

Figure 2c shows the difference in water table between DarcyLat_NoPump and CTRL simulations. Note that positive (negative) values mean deeper (shallower) water-level compared to CTRL. Evidently, the average water table depth across the eastern US remains within the range of −0.5 to +0.5 m difference from the CTRL simulation due to a small water table gradient between the grid cells. The relatively shallow water table in these regions causes the climate-induced vertical flux (recharge) to be balanced by large baseflow—as a function of water table depth—causing relatively small lateral flow compared to the recharge. Conversely, high water table gradients across the West and Southwest drive large regional groundwater flows between intermountain hills and valleys. The relatively deep water table in these regions causes small convergent baseflow compared to the recharge and lateral groundwater flow. Finally, the results shown as the difference between DarcyWellLat_Pump and CTRL_PumpNoLat simulations (Figure 2d) highly resemble Figure 2c for most areas. Exceptions are the managed aquifer systems where groundwater pumping causes large water level drop, analogous to that in CTRL_PumpNoLat; however, the lateral flow in DarcyWellLat_Pump allows intercell exchanges as a function of transmissivity and head gradient. The water-level gradient imposed by pumping can directly impact both magnitude and direction of the lateral flow. For example, a grid cell that discharges natural recharge flux to the neighbors in DarcyLat_NoPump could switch the role under pumping and receive lateral flow from its neighbors in DarcyWellLat_Pump.

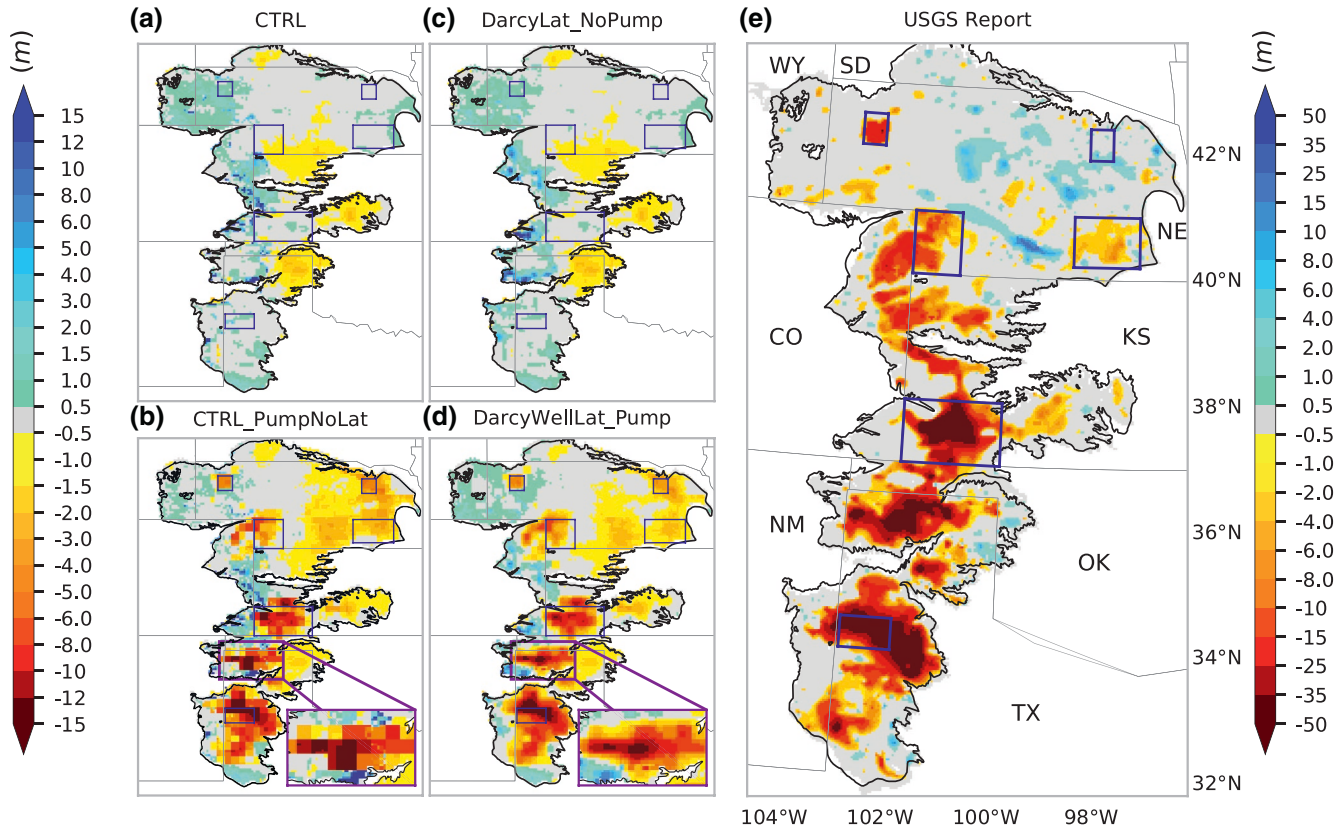

Figure 3. Cumulative groundwater-level change across the HPA for 2000–2015 period from simulations (a–d) compared with the USGS report, provided at 500 m resolution, for predevelopment period (~1950) to 2015 (e). Note that the CLM5 simulations (a–d) share the left color bar. Blue boxes show the regions of interest where temporal variation of groundwater-level is validated with USGS data (Figure 4). CLM5, Community Land Model version 5; HPA, High Plains Aquifer; USGS, US Geological Survey.

3.2. Groundwater-Level Change in the HPA and CVA

The spatiotemporal changes in water table depth due to irrigation pumping are examined for the HPA and CVA, the most heavily exploited aquifers in the US that rank first and second in terms of the groundwater withdrawals (Scanlon, Faunt, et al., 2012). The USGS continuously monitors the changes in groundwater-level across the HPA (with an area of ~450,000 km^2) before the irrigation season starts every year using over 3,000 wells (McGuire, 2011).

Figure 3 compares the spatial patterns of accumulated water-level change from simulations (a–d) and USGS report (e) (McGuire, 2017). The USGS report (Figure 3e) illustrates water-level changes from predevelopment (~1950) to 2015, which ranges from ~25-m increase in small regions in Nebraska to ~70-m depletion in Texas Panhandle. While the northeast HPA in Nebraska houses extensive irrigated areas (Felfelani et al., 2018), the USGS map shows little to no depletion in that region. Contrarily, patches of water-level increase can be seen in the north-central part of Nebraska (Figure 3e) due to increased recharge in recent times (Scanlon, Faunt, et al., 2012). Toward the south of HPA, the reported depletion reaches ~20 m at the border of Nebraska and Colorado, ~50 m in the southwest of Kansas and north border of Texas and exceeds 50 m in the southern HPA. In general, the north-to-south water-level gradient can be explained mainly by the low annual recharge, meaning that groundwater withdrawals are generally unsustainable in the central and southern HPA.

As seen in Figures 3a and 3c, the simulated water-level changes from CTRL and DarcyLat_NoPump present relatively similar spatial variability for 2000–2015 period; the changes in these simulations are climate-driven. These simulations fall short in capturing the reported depletion hotspots across the HPA by a large margin. A minor depletion of 0.5–1.5 m is discernible in northern Texas, central Kansas, and at the border

of Nebraska and Kansas, inconsistent with the critical regions seen in USGS data. Furthermore, the increasing water-level on the west side of HPA (CTRL and DarcyLat_NoPump) can be attributed to high recharge which is subsequently spread over a wider area by lateral flow (Figure 3c), governed by the water-level gradient and transmissivity.

Implementation of groundwater pumping in CTRL_PumpNoLat results in a significantly improved simulation of the accumulated water-level change (Figure 3b), capturing most of the hotspots of groundwater depletion in the central and southern regions. The groundwater drawdown in CTRL_PumpNoLat reaches ~8 m at the border of Colorado and Nebraska, ~13 m over the southwestern Kansas, and ~18 m in Texas Panhandle for 2000–2015 period. Differences between the USGS data and CTRL_PumpNoLat simulation can be primarily seen in Nebraska. While most of the regions with small water-level change (i.e., −0.5 to 0.5 m) in central and northern Nebraska and even the small region of large depletion in northwest of Nebraska are accurately simulated, ~0.5–5 m drawdown is simulated across the northeast and south-center of Nebraska that does not exist with a comparable spatial extent in the USGS data. The overestimated depletion in Nebraska can be associated with overestimation of irrigation water owing to the unrealistic setting of target soil moisture (Felfelani et al., 2018), the uncertainties in input data (e.g., irrigation fraction and crop types which impact the estimation of irrigation water requirement), and underestimation of recharge, especially irrigation return flow (i.e., due to soil hydrology and evapotranspiration processes).

While DarcyWellLat_Pump (Figure 3d) tends to include all improvements in capturing the depletion hotspots achieved in CTRL_PumpNoLat, the consideration of lateral flow based on the well equation along with pumping further enhances the simulation of groundwater-level change. The lateral flow mechanism partly compensates the pumping-induced storage depletion by allowing flow convergence from the neighboring grid cells and forming features resembling cones of depression (insets in Figures 3b and 3d), resulting in a smoothening of the pixelated groundwater-level change.

Figure 4 depicts the comparison of the simulated groundwater-level change with the annual winter time USGS observations (McGuire, 2014, 2017), along with monthly precipitation and shown for wells (i.e., filtered based on the criteria noted in Section 2.1 for the 75th percentile of long-term water-level mean) in regions of large depletion across the HPA (outlined by blue boxes in Figure 3). See Figure S3 for different regions selected and Figure S4 for the same zones as in Figure 4 but for the 50th percentile of long-term water-level mean. Consistent with the spatial patterns across the HPA (Figure 3), the CTRL, and DarcyLat_NoPump show relatively stable temporal patterns, as opposed to the USGS water-level changes that show a continuous fall-off from 2000 to 2013, especially in Kansas and Texas. High precipitation during 2007–2012 in Nebraska reduces groundwater loss, even resulting in water level increase by a few meters (NE_S and NE_NE). Among simulations, those with pumping (CTRL_PumpNoLat and DarcyWellLat_Pump) match most closely with the USGS data, not only over largely depleted regions (Figure 4, Figures S3 and S4) but also across regions that appear to recover from a major drawdown (e.g., northern HPA where high recharge balance irrigation water use; Figure 4 and Figure S5), indicating overall improvements in the simulation of groundwater dynamics (both spatial and temporal). While large groundwater depletion rates in NE_SW, NE_NW, and TX_NC (i.e., 4, 4, and 12 m declines for 2000–2013, respectively) are well replicated by CTRL_PumpNoLat and DarcyWellLat_Pump, water-level drawdown in KS_SW is slightly underestimated and in NE_NE is overestimated which could be related to various factors including errors in the amount of water extraction, biases in recharge likely caused by uncertainties in climate forcing, and soil hydrology parameterizations.

When aggregated over a relatively large region, the impact of lateral flow on the simulated groundwater-level change is found to be negligible in the absence of pumping (CTRL compared with DarcyLat_NoPump) and rather insignificant even when pumping is considered (CTRL_PumpNoLat compared with DarcyWellLat_Pump), due to the inherent and strong scale dependency of the lateral flow. Figures S6 and S7 provide contrasting examples of the differences between simulations with and without lateral flow at grid cell scale compared with single well data in different locations. Notable refinements can be observed in the simulations with lateral flow in both pumping and no-pumping cases across many cites (e.g., Figures S6a–S6f, S6m–S6o and Figures S7f, S7g, S7o, and S7p). However, there are also well locations where lateral flow tends to not improve the simulation (Figures S7b and S7n). Furthermore, errors and uncertainties in the input irrigation datasets could cause failure in capturing the groundwater loss (Figure S7h) and/or false trigger of irrigation (Figure S6l).

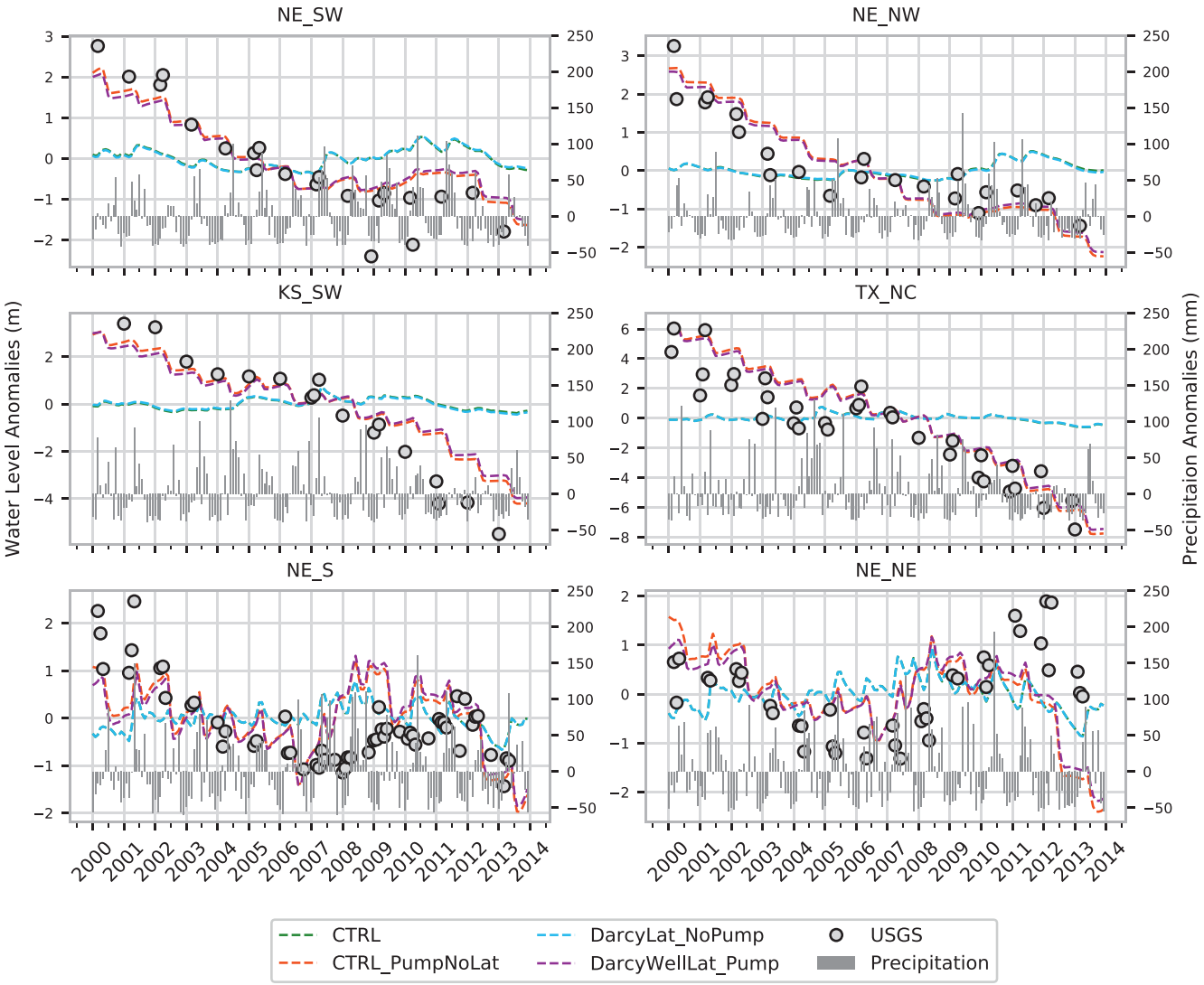

Figure 4. Time series of water-level anomalies from simulations compared with the well data for selected regions within the HPA (blue boxes in Figure 3). In total, data from 366 wells in southern Nebraska (NE_S), 31 wells in southwest of Nebraska (NE_SW), 32 wells in southwest of Kansas (KS_SW), 23 wells in north-center of Texas (TX_NC), 14 wells in northeast of Nebraska (NE_NE), and 9 wells in northwest of Nebraska (NE_NW) are used in the analysis. Bars show the monthly total precipitation as anomalies. CTRL, control experiment; HPA, High Plains Aquifer; USGS, US Geological Survey.

The CVA with an area of ~52,000 km^2 includes the Sacramento Valley in the north, the San Joaquin Valley in the middle, and the Tulare Basin in the south. Unlike in the HPA, surface water accounts for a large fraction (~50%) of irrigation water over this arid to semiarid region (Bertoldi, 1989).

Figure 5 compares the water-level changes from simulations (a–d) accumulated over 2000–2015 period with the USGS estimated changes (e) from the predevelopment (~1860) to 1961 across CVA (Bertoldi et al., 1991; Williamson et al., 1989). Note that the simulation period in this study lies entirely after the period in USGS report (~1860–1961), however, since the intensive groundwater pumping across CVA began more than a century ago and has been maintained until now, it is reasonable to expect relatively similar spatial patterns of groundwater drawdown over time. Furthermore, due to data limitations (e.g., lack of USGS continuous monitoring of groundwater-level changes similar to the HPA), this is the only comparison that could be made (de Graaf et al., 2019).

According to the USGS estimate, the maximum depletion (i.e., 12–120 m) has occurred in the Tulare Basin in the southern CVA with the highest depletion rate on the west (Scanlon, Longuevergne, et al., 2012). The water-level declines in the Sacramento and San Joaquin Valleys are less severe, ranging from 0 to 24 m,

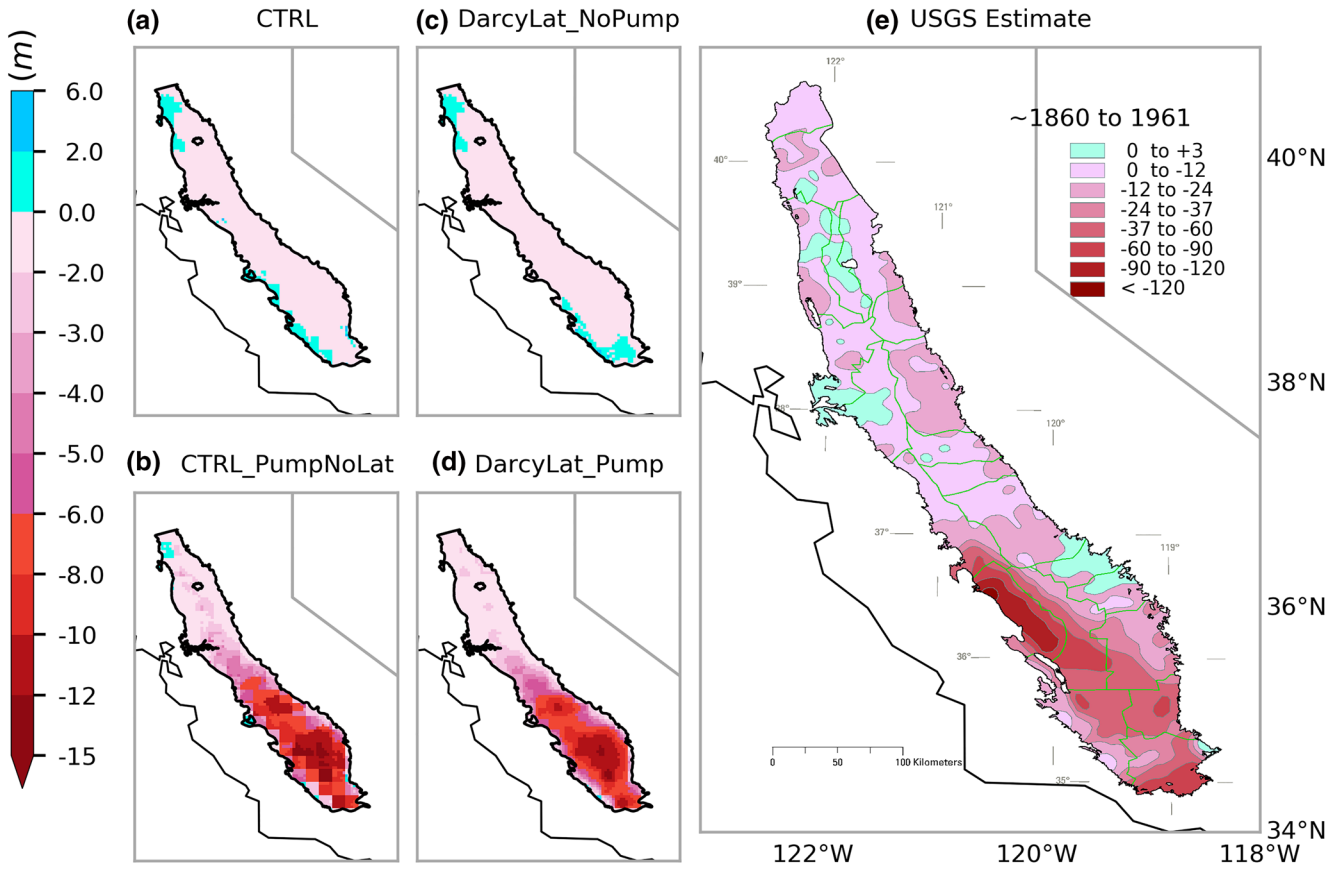

Figure 5. Cumulative groundwater-level change across the CVA for 2000–2015 period from simulations (a–d) compared with the USGS estimated water-level change for predevelopment period (~1860) to 1961 (modified from Faunt, 2009; Williamson et al., 1989) (d). Note that the simulations (a–d) share the left color bar. CTRL, control experiment; CVA, Central Valley Aquifer; USGS, US Geological Survey.

and even small regions of water-level rise of ~3 m can be seen, for example, in the Delta on the west. In the absence of groundwater extraction and lateral flow, the CTRL simulation only reflects the vertical climate-driven water-level changes (Figure 5a), showing declines of less than 2 m in the valleys, mainly due to prolonged drought and reduced recharge, and rises in the range of 0–2 m in the surrounding areas with higher elevation and precipitation.

Similar to the HPA case, the DarcyLat_NoPump simulation (Figure 5c) compares favorably with the CTRL with a relatively small (0–2 m) groundwater decline across most of the CVA and 0–2 m increase at its northern and southern parts; however, lateral flow extends the groundwater depletion/rise in DarcyLat_NoPump. The results from the CTRL_PumpNoLat and DarcyWellLat_Pump (Figures 5b and 5d) suggest an overall improvement in the simulation of groundwater-level changes in the CVA. The higher rate of simulated water-level drop toward the southern San Joaquin Valley and central Tulare Basin matches with the USGS estimate and the findings from other studies (de Graaf et al., 2019; Scanlon, Longuevergne, et al., 2012; Williamson et al., 1989). However, the largest depletion (~12 m) is simulated around the center of the Tulare Basin, slightly shifted compared to the maximum depletion location seen in the USGS data (Figure 5e). Contribution of lateral flow in DarcyWellLat_Pump shows promise in smoothening the pixelated spatial distribution of the change in groundwater level (Figure 5b), a potential model artifact, and forming even a cone of depression similar to the HPA case. Finally, small declines (~0–2 m) in the water-level are simulated in the Sacramento Valley region which show good consistency with the observations.

To better investigate how large-scale pumping impacts groundwater movement, we present the lateral groundwater flow fields from the simulations with (DarcyWellLat_Pump) and without (DarcyLat_NoPump) pumping. For this purpose, the lateral fluxes from all eight neighboring cells are projected onto the

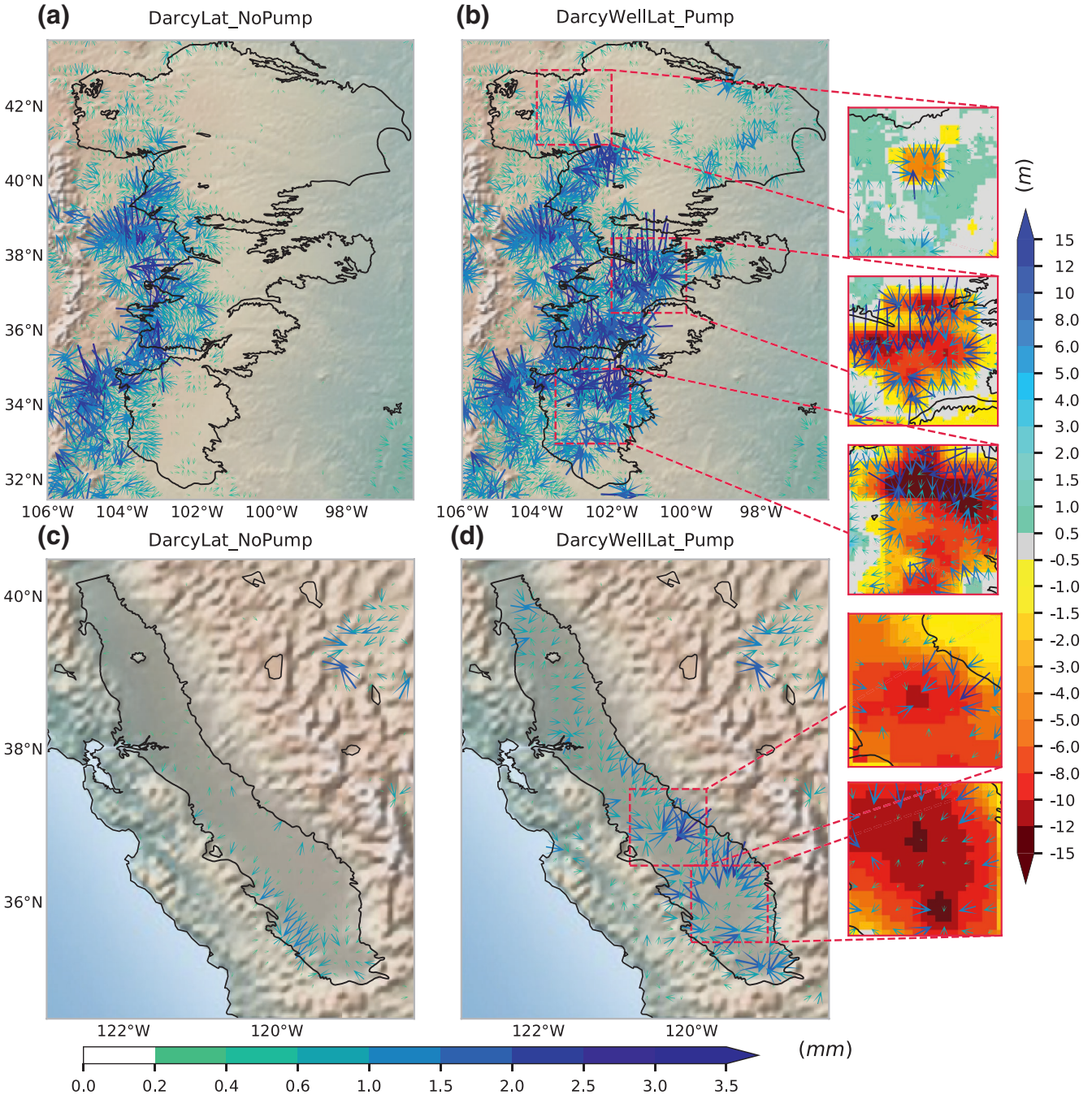

Figure 6. Mean lateral flow fields over the HPA (a and b) and CVA (c and d) for 2000–2016. Background shows the surface elevation as a shaded relief image. Regions of large depletion are presented as insets in the right, showing lateral groundwater flow vectors in the foreground of cumulative groundwater-level change (Figures 3 and 5).

coordinate axes, aggregated on the four edges of grid cells, and then averaged for both vertical and horizontal directions to get the north-south and east-west components at the center of the cell. These components are then used to show the mean lateral flow fields for 2000–2016 period across the HPA and CVA (Figure 6). While the lateral fluxes in the DarcyLat_NoPump simulation (Figures 6a and 6c) are controlled by recharge (e.g., in the west border of HPA) and topography (e.g., southwest of CVA), irrigation-pumping imposes large water table gradient and lateral influxes (i.e., up to 3.5 mm month^{-1}) toward the cones of depression in the two aquifers (zoomed-up insets in Figures 6b and 6d). For example, the most depleted regions in central

and southern HPA (Figure 3d) and southern CVA (Figure 5d) receive relatively high lateral flows—modulated by the aquifer transmissivity—from the surrounding areas. Furthermore, climate variability could also affect the magnitude of lateral flow. For example, relatively higher lateral flow can be expected during wet years compared to dry years. These results underscore the importance of lateral flow at the grid scale used in this study and especially when pumping is considered.

The significance of the intercell lateral flow (i.e., relative to the grid water budget) has been defined in both relative (exceeding 10% of recharge) and absolute terms (exceeding 10 mm year^{-1}) (Krakauer et al., 2014). Results from the DarcyLat_NoPump simulation (Figure S8) suggest that in over 30% of the total land areas within the study domain, the contribution of lateral flow is significant when the relative criterion is considered. This percentage increases to 32% in DarcyWellLat_Pump, where the pumping-induced head gradient triggers a higher lateral flow in the pumping cells. Furthermore, the sensitivity of the intercell lateral flow across spatial scales is quantified by aggregating the area-averaged lateral flow at 3 arc-min resolution into 0.125° and 0.5° resolutions (Figures S9 and S10). The area with significant contribution of lateral flow reduces from 32% (DarcyWellLat_Pump) to 29% and 15%, respectively, at 0.125° and 0.5° resolutions.

The magnitude of lateral flow is highly dependent on transmissivity; low conductivities can impose significant resistance to lateral flow (de Graaf et al., 2020). Improved representation of bedrock (e.g., by considering bedrock and alluvial aquifers interconnectivity; Raiber et al., 2019), aquifer thickness, and conductivity in LSMs using emerging global datasets (e.g., de Graaf et al., 2020; Gleeson et al., 2014; Huscroft et al., 2018) could potentially influence the water balance and help address groundwater related issues in modeling. Finally, the constant soil thickness is another structural shortcoming in this study. While setting a limitation on soil thickness is unavoidable in large-scale modeling to reduce the computation cost, unrealistic constant soil thickness would introduce bias in soil moisture simulation, and consequently in head-based recharge representation. As such, the depth-to-bedrock data set could be incorporated to restrict water table depth and to allow for variable soil thickness across regions with shallow depth-to-bedrock (i.e., shallower than 8.5 m).

3.3. Decadal Water Storage Trends

Figure 7 presents a comparison of spatial variability in TWS trend from simulations and GRACE data across the CONUS for 2005–2015 period. This period is selected to represent strong positive and negative decadal trends in TWS with the emphasis on hotspots of groundwater depletion (see Figure S11 for 2002–2016 trend maps). For better comparison with coarse resolution GRACE data, TWS simulations with 3 arc-min resolution are transformed to SH domain, truncated at degree and order 60, and smoothed by the 300-km Gaussian filter, similar to the postprocessing applied to GRACE SH products (Felfelani et al., 2017; Long et al., 2015; Longuevergne et al., 2010; Wahr et al., 1998). Consistent with the fact that the significance of lateral groundwater flow is inversely related to the grid resolution (Krakauer et al., 2014), the contribution of lateral flow to TWS becomes relatively insignificant at the GRACE spatial scale, especially after the application of the 300-km Gaussian filter. Therefore, the results from CTRL and CTRL_PumpNoLat are not shown as those resemble the DarcyLat_NoPump and DarcyWellLat_Pump, respectively, in most regions.

GRACE data show large negative trends in TWS (Figures 7a–7c) that mostly overlap with the irrigation hot spots, suggesting that irrigation plays a major role in modulating TWS in these regions. There are also large negative trends over nonirrigated areas detected by GRACE (e.g., across the northwestern Great Lakes region), mainly driven by natural variabilities. Conversely, GRACE shows large positive TWS trends across the Southeast and northern half of the CONUS. Specifically, TWS increases in the northern HPA (Figures 7a–7c), in line with the USGS observation of groundwater rises in these highly irrigated regions (Figure 3e). In general, the spatial variability of decadal trends in TWS from simulations (Figures 7d and 7e) shows close correspondences among the simulations and good agreement with GRACE (Figures 7a–7c) in terms of the magnitude and direction of change. However, certain discrepancies are apparent mainly in terms of the magnitude between GRACE and simulations, among simulations, and even among different GRACE products, especially in regions with relatively high human influence (e.g., CVA and HPA). As a counterexample, there are also few regions with relatively low human impacts (e.g., across the East and Southeast) where GRACE and simulations show contradictory direction of change in TWS. A good correlation between the direction of change in TWS simulations and NLDAS precipitation (not shown) implies

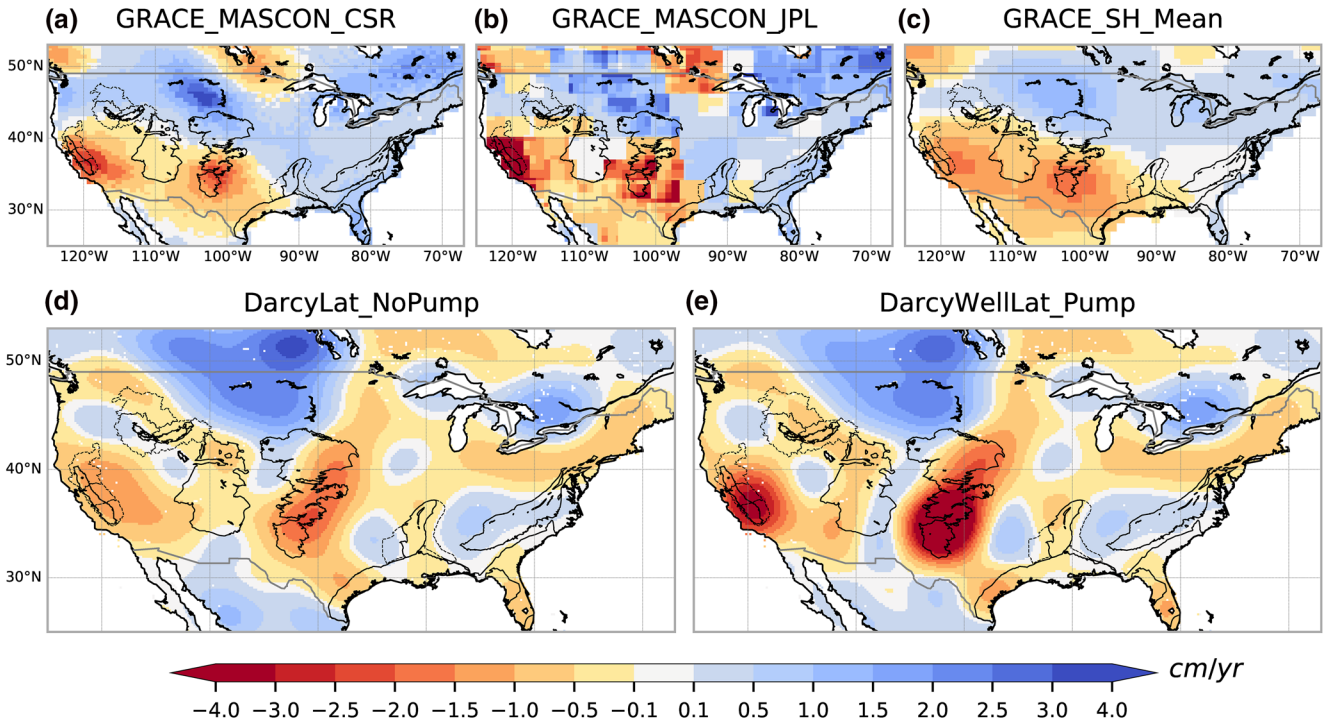

Figure 7. Spatial distribution of TWS trends (cm year^{-1}) based on 0.5° GRACE CSR (a) and JPL (b) mascon solutions, the mean of one-degree SH solutions from CSR, JPL, and GFZ centers (c), and 3 arc-min simulations (d and e) for 2005–2015. Scaling factors are applied to GRACE JPL mascon anomalies to downscale its resolution to 0.5° × 0.5°. Major US aquifers are shown with solid black line for which the average trend values are provided in Table 2. For the aquifers with areas smaller than the GRACE footprint of ~200,000 km^2 (i.e., CVA, Mississippi Alluvial Plain, and Snake River Plain), larger hydrological units shown by dashed line are considered for trend calculations. CSR, Center for Space Research; GFZ, German Research Center for Geoscience; GRACE, Gravity Recovery and Climate Experiment; JPL, Jet Propulsion Laboratory; SH, spherical harmonic; TWS, terrestrial water storage.

that the differences between GRACE data and model results across the East could partly be due to the biases in forcing data, especially precipitation.

The DarcyLat_NoPump (Figure 7d) tends to capture the negative and positive trends with the magnitudes and extents analogous to that of the GRACE data. For example, agreements across the Southwest, north-central US, and northwest of HPA, where lateral flow can be seen (Figure 3c) to spread over the high recharge on the west border of HPA, are discernible. Furthermore, the DarcyWellLat_Pump simulation (Figure 7e) resembles DarcyLat_NoPump in most of the regions, except for areas with large groundwater-supplied irrigation. The DarcyWellLat_Pump simulation shows improved agreement (i.e., compared to DarcyLat_NoPump) in capturing the GRACE-detected downward trend in areas such as the CVA, however, it also overestimates the pumping-induced TWS depletion rate (e.g., over the HPA) compared to GRACE.

Considering the coarse spatial resolution of GRACE data and postprocessing (e.g., Gaussian and de-striping filtering applied to the SH products), comparison of the modeled TWS and GRACE data could suffer from inherent uncertainties, especially in dry regions with localized human water abstractions (Döll, Fritsche, et al., 2014). We also show the disparities between the GRACE products (Figures 7a–7c), which could partly explain the aforementioned uncertainties. For example, mascon solutions depict relatively large negative TWS trends (~1–5 cm year^{-1}) over the southwestern and western US including the CVA, southern HPA, and the Coastal Lowlands Aquifer (Figures 7a and 7b). Similarly, GRACE SH products (Figure 7c) shows negative trends across the southern US, however, the signals are rather attenuated. There are also notable discrepancies, including even opposite signs of change, between different GRACE products (e.g., over the Great Lakes region). These results suggest that the GRACE uncertainties must be considered when evaluating TWS simulations.

Table 2 provides the decadal trends in TWS for the major US aquifers from simulations and GRACE products for 2005–2015 period (see Table S1 for 2002–2016 period). Similar to Figure 7, the lateral flow contribution to

Table 2
Decadal Trends (cm year^{-1}; 2005–2015 Period) in TWS for the Major US Aquifers

Aquifer name	Test	CTRL	CTRL_ PumpNoLat	DarcyLat_ NoPump	DarcyWellLat_ Pump	GRACE CSR	GRACE JPL	GRACE SH mean
Central Valley[a]	Wald	−1.080* ± 0.17	−2.205* ± 0.17	−1.087* ± 0.17	−2.153* ± 0.17	−1.772* ± 0.25	−3.457* ± 0.29	−1.286*
	M-K	−1.024*	−2.155*	−1.032*	−2.106*	−1.873*	−3.808*	−1.412*
High Plains	Wald	−0.878* ± 0.10	−2.355* ± 0.12	−0.893* ± 0.10	−2.298* ± 0.13	−0.226 ± 0.11	−0.489* ± 0.11	−0.507*
	M-K	−0.835*	−2.296*	−0.847*	−2.233*	−0.199	−0.442*	−0.478*
Mississippi Alluvial Plain[b]	Wald	−0.120 ± 0.24	−0.198 ± 0.26	−0.119 ± 0.24	−0.191 ± 0.26	0.202 ± 0.28	0.412 ± 0.35	−0.294
	M-K	−0.074	−0.174	−0.071	−0.170	0.226	0.531	−0.284
Piedmont Blue Ridge	Wald	0.110 ± 0.19	0.096 ± 0.19	0.113 ± 0.19	0.095 ± 0.19	0.425* ± 0.17	0.431* ± 0.17	0.059
	M-K	0.075	0.062	0.080	0.057	0.406	0.354	0.028
Coastal Lowlands	Wald	−0.262 ± 0.13	−0.381* ± 0.13	−0.255 ± 0.13	−0.377* ± 0.13	−0.030 ± 0.14	−0.110 ± 0.16	−0.450*
	M-K	−0.269	−0.390*	−0.264	−0.382*	−0.057	−0.101	−0.464*
Surficial	Wald	−0.354* ± 0.10	−0.375* ± 0.11	−0.353* ± 0.10	−0.357* ± 0.11	0.924* ± 0.11	0.626* ± 0.18	0.167
	M-K	−0.326*	−0.344*	−0.328*	−0.330*	0.949*	0.649*	0.149
Colorado Plateau	Wald	−0.290* ± 0.09	−0.329* ± 0.09	−0.362* ± 0.09	−0.348* ± 0.09	−0.251* ± 0.08	−0.156 ± 0.09	−0.834*
	M-K	−0.244*	−0.284*	−0.320*	−0.302*	−0.267*	−0.168	−0.885*
Snake River Plain[c]	Wald	−0.175 ± 0.15	−0.439* ± 0.15	−0.193 ± 0.15	−0.428* ± 0.16	0.211 ± 0.19	−0.035 ± 0.19	−0.184
	M-K	−0.138	−0.406*	−0.155	−0.397*	0.285	0.036	−0.178

Notes. The significance of trends is evaluated based on Wald and Mann-Kendall tests. Stars indicate that the trend is significantly different from zero at the 5% significance level.

Abbreviation: CTRL, control experiment; CSR, Center for Space Research; GRACE, Gravity Recovery and Climate Experiment; JPL, Jet Propulsion Laboratory; SH, spherical harmonic; TWS, terrestrial water storage.

[a]Sacramento, San Joaquin, and Tulare basins combined. [b]Mississippi Alluvial Plain and Mississippi Embayment combined. [c]Snake River Basin (upper, middle, and lower combined).

TWS is relatively insignificant at the basin scale; trends from CTRL and CTRL_PumpNoLat resemble those from DarcyLat_NoPump and DarcyWellLat_Pump, respectively. For many of the aquifers with decreasing TWS trend in GRACE data (i.e., HPA, Coastal Lowlands, Snake River Plain, and Mississippi Alluvial Plain), CTRL and DarcyLat_NoPump simulations outperform those with pumping in estimating the magnitude of change. Furthermore, the CTRL_PumpNoLat and DarcyWellLat_Pump perform better in CVA, but tend to overestimate the negative trend in HPA, consistent with the spatial patterns of TWS trend (Figures 7d and 7e). This difference in performance of pumping simulations can be explained partly by the larger contribution of groundwater to the total irrigation water withdrawal in the HPA (~90%) compared to that in the CVA (~40%; Figure S1), prescribed as model input. Our results also confirm that the HPA shows the largest pumping-induced TWS change (−1.457 cm year^{-1}), followed by the CVA (−0.994 cm year^{-1}) and Snake River Plain (−0.195 cm year^{-1}). Overall, the representation of lateral flow in CLM allows regional groundwater flow and tends to improve the subsurface response to TWS changes in certain regions (Table 2), although the impact is less significant at the coarse resolution of GRACE data. Finally, results from the seasonal cycle of TWS variations (Figure S12) show that the inclusion of pumping could increase the seasonal amplitude toward better agreement with GRACE.

Table 3 compares the irrigation water requirement and withdrawals from CTRL_PumpNoLat and DarcyWellLat_Pump (simulations that account for conjunctive water use) with the county-level data of irrigation water withdrawals across the HPA (Dieter et al., 2018; Maupin et al., 2014).

In the USGS data, irrigation water withdrawals in HPA range from 19.7 to 26.5 km^3 year^{-1} during 2000–2015, of which more than 88% on average has been extracted from groundwater (Table 3). Results from the CTRL_PumpNoLat and DarcyWellLat_Pump simulations suggest the irrigation water requirement to range from 17 to 25 km^3 year^{-1} for 2000–2015, of which only ~1–1.5 km^3 year^{-1} is withdrawn from surface water; the rest is supplied by groundwater (Table 3), consistent with the USGS data. For example, in year

Table 3
Comparison of Irrigation Water Withdrawals Over the HPA From the CTRL_PumpNoLat and DarcyWellLat_Pump Simulations With the USGS Data

	USGS (km^3 $year^{-1}$)		CTRL_PumpNoLat (km^3 $year^{-1}$)				DarcyWellLat_Pump (km^3 $year^{-1}$)			
Year	Irrigation withdrawal	GW source	IWR	Total withdrawal	GW source	SW source	IWR	Total withdrawal	GW source	SW source
2015	19.7	17.5	17.06	16.68	15.63	1.05	17.05	16.69	15.63	1.06
2010	19.8	16.8	19.22	18.88	17.82	1.07	19.21	18.88	17.81	1.07
2005	24.6	22.3	22.30	21.85	20.62	1.23	22.26	21.82	20.59	1.24
2000	26.5	23.6	24.56	23.94	22.46	1.48	24.40	23.77	22.32	1.45

Abbreviations: CTRL, control experiment; GW, groundwater; HPA, High Plains Aquifer; IWR, irrigation water requirement; SW, surface water; USGS, US Geological Survey.

2000, 23.77 out of 24.40 km^3 is extracted from groundwater (94%) and 1.45 km^3 is extracted from surface water (6%) in the DarcyWellLat_Pump simulation. Similar proportions are found in other years. While in CTRL and DarcyLat_NoPump, surface water is the sole source for irrigation and the majority of irrigation water requirement is supplied by an unlimited virtual source (i.e., due to the inadequate water in the main river channel and/or constraining surface water supply to the surface water contribution in the USGS data) which results in an unrealistic representation of irrigation. Therefore, it can be concluded that accounting for conjunctive use of groundwater and surface water for irrigation could largely improve the simulation of irrigation withdrawals (Table 3), groundwater dynamics, and aquifer depletion (Figures 3–5, Figures S3–S7) across the irrigated regions, but could also lead to an overestimation of TWS depletion (i.e., after the incorporation of pumping) compared to the GRACE data (specifically where groundwater is the major irrigation source). Such overestimation in regions with heavy irrigation-pumping has been reported also in other studies that used other models (e.g., HiGW-MAT, Noah-MP) with different irrigation and groundwater schemes (Nie et al., 2018; Pokhrel et al., 2015), remaining as an outstanding issue to be addressed in future studies.

3.4. River Discharge Simulation by MOSART

Finally, we evaluate the simulation of river discharge, an important hydrologic variable from water resource perspective that is tightly linked to groundwater dynamics. We test if the differences in the simulation of groundwater dynamics and baseflow generation from CTRL, CTRL_PumpNoLat, DarcyLat_NoPump, and DarcyWellLat_Pump would alter surface water routing by MOSART in CLM5, and whether the impact of pumping is apparent in streamflow simulations. For this purpose, MOSART simulations are compared with the USGS streamflow observations at downstream locations of the major river basins across CONUS (Figure 8; Table S2).

A good agreement is found between the simulated river discharge in the CTRL and DarcyLat_NoPump simulations and USGS observations (e.g., Columba River, Mississippi River, Illinois River, Ohio River, and Wabash River), specifically in the basins with relatively low human influence. This is obvious because MOSART currently does not account for reservoir operation. The performance of CTRL and DarcyLat_NoPump is further improved by activating pumping in the CTRL_PumpNoLat and DarcyWellLat_Pump simulations in most of the stations (e.g., Arkansas River, White River, Missouri River, Mississippi River), however, the improvements are not substantial (i.e., compared to CTRL and DarcyLat_NoPump) in terms of reproducing the observed seasonal cycle (Table S2). Furthermore, the differences between the simulations—which use the exponential decay formula for baseflow generation—are not always obvious, again in terms of the seasonal cycle (e.g., Susquehanna River, Ohio River).

In general, model overestimation in many of basins/catchments could be attributed to the lack of water withdrawals for other sectors than agriculture (e.g., industrial, domestic, thermoelectric power), absence of reservoir operation, and systematic biases in ET, irrigation return flow, and forcing data. Furthermore, the small difference in river discharge among different simulations highlights the fact that: (1) inclusion of

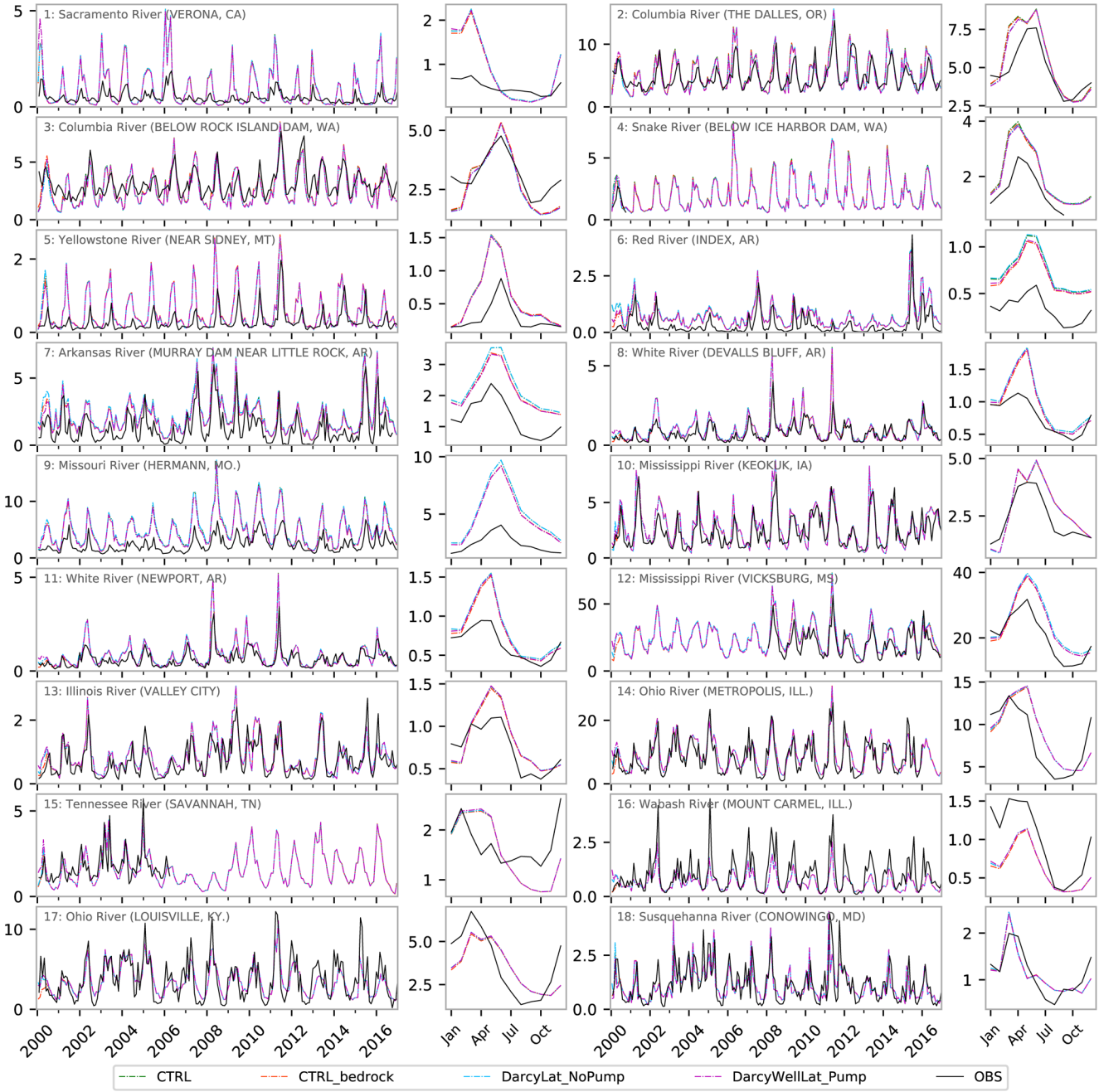

Figure 8. Comparison of simulated river discharge (10^3 m^3 s^{-1}) with the USGS streamflow data at the major gauging stations across the US. See Table S2 for statistical measures. USGS, US Geological Survey.

lateral flow and groundwater pumping does not substantially alter river discharge simulations over large basins (e.g., Mississippi River, Ohio River), especially at the current model grid of ~13 km, (2) the impact of pumping was minimal because pumping occurs mostly in semiarid and dry regions where the water table is relatively deep and has low impact on river flow (again, at the current model grid and spatial extent) (Winter et al., 1998), and (3) the subsurface runoff parameters (i.e., $q_{drai,max}$ and f_{drai}) are not specifically calibrated for the selected basins and hence are not highly sensitive to groundwater table depth that characterized the primary difference between the four simulations (Bisht et al., 2018). It is expected that by increasing the

MOSART resolution and calibrating the subsurface runoff parameters, the direct impact of lateral flow and pumping on the river discharge could be better represented.

4. Conclusions

A new prognostic groundwater scheme, which accounts for lateral groundwater flow and conjunctive use of groundwater and surface water for irrigation, is implemented in the latest version of CLM (CLM5). Four sets of simulations (all combinations by turning lateral flow and pumping on and off) are conducted at 5-km grids and over the CONUS. To simulate groundwater pumping for irrigation use, we introduce—for the first time—an explicit representation of the steady-state well equation in LSMs. Results show that the new groundwater model significantly improves the simulation of groundwater-level change and promisingly captures most of the hotspots of groundwater depletion across the HPA and CVA, the most heavily exploited aquifers in the US. While the simulations equipped with pumping improve TWS over CVA and river discharge in most of the major river basins across the US, they tend to overestimate TWS depletion rate, especially across HPA where groundwater supplies the majority of irrigation water use. Furthermore, incorporation of lateral flow results in improved subsurface response to pumping (i.e., by smoothening the pixelated groundwater-level change to form a cone of depression) as well as natural wet and dry cycles; however, the impact is not substantial at the basin scale or coarse grids. There are certain limitations to this study that open avenues for future work. First, the use of newly available datasets that describe global aquifer properties such as the global permeability and depth-to-bedrock datasets could improve the representation of lateral flow and pumping. Second, it is essential to further assess uncertainties in the GRACE products over high-depletion regions. Third, inclusion of lateral flow and pumping is expected to have larger impacts on river discharge that may require spatial calibration of the subsurface runoff parameters. Future studies could also consider water withdrawals for all sectors and include reservoir operation in the river routing scheme. Lastly, the uncertainties arising from forcing data could be quantified using ensemble simulations with multiple forcing datasets. Despite these limitations, this study provides important advances in simulating groundwater dynamics in LSMs by considering lateral flow, aquifer pumping, and conjunctive water use for irrigation.

Data Availability Statement

All data used to generate the major figures are publicly available on CUAHSI HydroShare. The USGS irrigation and groundwater use data are available at: https://water.usgs.gov/watuse/data/index.html; GRACE data are available at: https://podaac.jpl.nasa.gov/GRACE; USGS observational wells data are available at: https://ne.water.usgs.gov/projects/HPA/data.html.

Acknowledgments
This study was supported in part by the National Science Foundation (NSF CAREER Award; grant #: 1752729). Simulations were conducted using computing resources from the High Performance Computing Center (HPCC) provided by the Michigan State University and Cheyenne doi:(https://doi.org/10.5065/D6RX99HX) provided by NCAR's Computational and Information Systems Laboratory, sponsored by the NSF. The authors thank Shu-Guang Li, Phanikumar Mantha, and Kyla Dahlin for providing helpful comments and suggestions. This material is based upon work supported by the National Center for Atmospheric Research, which is a major facility sponsored by the NSF under Cooperative Agreement No. 1852977. DML is also supported by the National Institute of Food and Agriculture/US Department of Agriculture grant 2015-67003-23489.

References

Anderson, M. P., Woessner, W. W., & Hunt, R. J. (2015). *Applied groundwater modeling: Simulation of flow and advective transport*, London, UK: Academic Press.

Bertoldi, G. L. (1989). *Ground-water resources of the Central Valley of California* (USGS Numbered Series No. 89–251). Washington, DC: Department of the Interior, US Geological Survey. Retrieved from http://pubs.er.usgs.gov/publication/ofr89251

Bertoldi, G. L., Johnston, R. H., & Evenson, K. D. (1991). *Ground water in the Central Valley, California: A summary report* (USGS Numbered Series No. 1401-A). Washington, DC: US Geological Survey Professional Paper 1401-A. Retrieved from http://pubs.er.usgs.gov/publication/pp1401A

Bierkens, M. F. P., Bell, V. A., Burek, P., Chaney, N., Condon, L. E., David, C. H., et al. (2015). Hyper-resolution global hydrological modelling: What is next?. *Hydrological Processes*, *29*(2), 310–320. https://doi.org/10.1002/hyp.10391

Bisht, G., Riley, W. J., Hammond, G. E., & Lorenzetti, D. M. (2018). Development and evaluation of a variably saturated flow model in the global E3SM Land Model (ELM) version 1.0. *Geoscientific Model Development*, *11*(10), 4085–4102. https://doi.org/10.5194/gmd-11-4085-2018

Chaney, N. W., van Huijgevoort, M. H. J., Shevliakova, E., Malyshev, S., Milly, P. C. D., Gauthier, P. P. G., & Sulman, B. N. (2018). Harnessing big data to rethink land heterogeneity in Earth system models. *Hydrology and Earth System Sciences*, *22*(6), 3311–3330. https://doi.org/10.5194/hess-22-3311-2018

Chaudhari, S., Pokhrel, Y., Moran, E., & Miguez-Macho, G. (2019). Multi-decadal hydrologic change and variability in the Amazon River basin: Understanding terrestrial water storage variations and drought characteristics. *Hydrology and Earth System Sciences*, *23*(7), 2841–2862. https://doi.org/10.5194/hess-23-2841-2019

Condon, L. E., & Maxwell, R. M. (2015). Evaluating the relationship between topography and groundwater using outputs from a continental-scale integrated hydrology model. *Water Resources Research*, *51*(8), 6602–6621. https://doi.org/10.1002/2014WR016774

Condon, L. E., & Maxwell, R. M. (2019). Simulating the sensitivity of evapotranspiration and streamflow to large-scale groundwater depletion. *Science Advances*, *5*(6), eaav4574. https://doi.org/10.1126/sciadv.aav4574

Cuthbert, M. O., Taylor, R. G., Favreau, G., Todd, M. C., Shamsudduha, M., Villholth, K. G., et al. (2019). Observed controls on resilience of groundwater to climate variability in sub-Saharan Africa. *Nature*, *572*(7768), 230–234. https://doi.org/10.1038/s41586-019-1441-7

Danabasoglu, G., Lamarque, J.-F., Bacmeister, J., Bailey, D. A., DuVivier, A. K., Edwards, J., et al. (2020). The Community Earth System Model version 2 (CESM2). *Journal of Advances in Modeling Earth Systems*, *12*(2), e2019MS001916. https://doi.org/10.1029/2019MS001916

de Graaf, I. E. M., Condon, L., & Maxwell, R. (2020). Hyper-resolution continental-scale 3-D aquifer parameterization for groundwater modeling. *Water Resources Research*, *56*(5), e2019WR026004. https://doi.org/10.1029/2019WR026004

de Graaf, I. E. M., Gleeson, T., van Beek, L. P. H., Sutanudjaja, E. H., & Bierkens, M. F. P. (2019). Environmental flow limits to global groundwater pumping. *Nature*, *574*(7776), 90–94. https://doi.org/10.1038/s41586-019-1594-4

de Graaf, I. E. M., Sutanudjaja, E. H., van Beek, L. P. H., & Bierkens, M. F. P. (2015). A high-resolution global-scale groundwater model. *Hydrology and Earth System Sciences*, *19*(2), 823–837. https://doi.org/10.5194/hess-19-823-2015

de Graaf, I. E. M., van Beek, R. L. P. H., Gleeson, T., Moosdorf, N., Schmitz, O., Sutanudjaja, E. H., & Bierkens, M. F. P. (2017). A global-scale two-layer transient groundwater model: Development and application to groundwater depletion. *Advances in Water Resources*, *102*, 53–67. https://doi.org/10.1016/j.advwatres.2017.01.011

Devanand, A., Huang, M., Ashfaq, M., Barik, B., & Ghosh, S. (2019). Choice of irrigation water management practice affects Indian summer monsoon rainfall and its extremes. *Geophysical Research Letters*, *46*(15), 9126–9135. https://doi.org/10.1029/2019GL083875

Dieter, C. A., Maupin, M. A., Caldwell, R. R., Harris, M. A., Ivahnenko, T. I., Lovelace, J. K., et al. (2018). *Estimated use of water in the United States in 2015* (Supersedes USGS Open-File Report 2017-1131, Circular 1441, pp. 1–65). Reston, VA: US Geological Survey. https://doi.org/10.3133/cir1441

Döll, P., Fritsche, M., Eicker, A., & Müller Schmied, H. (2014). Seasonal water storage variations as impacted by water abstractions: Comparing the output of a global hydrological model with GRACE and GPS observations. *Surveys in Geophysics*, *35*(6), 1311–1331. https://doi.org/10.1007/s10712-014-9282-2

Döll, P., Hoffmann-Dobrev, H., Portmann, F. T., Siebert, S., Eicker, A., Rodell, M., et al. (2012). Impact of water withdrawals from groundwater and surface water on continental water storage variations. *Journal of Geodynamics*, *59*(60), 143–156. https://doi.org/10.1016/j.jog.2011.05.001

Döll, P., Müller Schmied, H., Schuh, C., Portmann, F. T., & Eicker, A. (2014). Global-scale assessment of groundwater depletion and related groundwater abstractions: Combining hydrological modeling with information from well observations and GRACE satellites. *Water Resources Research*, *50*(7), 5698–5720. https://doi.org/10.1002/2014WR015595

Fan, Y., Clark, M., Lawrence, D. M., Swenson, S., Band, L. E., Brantley, S. L., et al. (2019). Hillslope hydrology in global change research and earth system modeling. *Water Resources Research*, *55*(2), 1737–1772. https://doi.org/10.1029/2018WR023903

Fan, Y., Li, H., & Miguez-Macho, G. (2013). Global patterns of groundwater table depth. *Science*, *339*(6122), 940–943. https://doi.org/10.1126/science.1229881

Fan, Y., Miguez-Macho, G., Weaver, C. P., Walko, R., & Robock, A. (2007). Incorporating water table dynamics in climate modeling: 1. Water table observations and equilibrium water table simulations. *Journal of Geophysical Research*, *112*(D10), D10125. https://doi.org/10.1029/2006JD008111

Faunt, C. C. (2009). *Groundwater availability of the Central Valley aquifer, California* (USGS Professional Paper 1766, USGS Numbered Series, pp. 1–225). Reston, VA: US Geological Survey. Retrieved from https://pubs.usgs.gov/pp/1766/

Feddes, R. A., Kabat, P., Van Bakel, P. J. T., Bronswijk, J. J. B., & Halbertsma, J. (1988). Modelling soil water dynamics in the unsaturated zone—State of the art. *Journal of Hydrology*, *100*(1), 69–111. https://doi.org/10.1016/0022-1694(88)90182-5

Feinstein, D. T., Fienen, M. N., Reeves, H. W., & Langevin, C. D. (2016). A semi-structured MODFLOW-USG model to evaluate local water sources to wells for decision support. *Ground Water*, *54*(4), 532–544. https://doi.org/10.1111/gwat.12389

Felfelani, F. (2019). *Improving the representation of irrigation and groundwater in global land surface models to advance the understanding of hydrology-human-climate interactions*, East Lansing, MI: ProQuest, Michigan State University. Retrieved from http://gateway.proquest.com/openurl?url_ver=Z39.88-2004&rft_val_fmt=info:ofi/fmt:kev:mtx:dissertation&res_dat=xri:pqm&rft_dat=xri:pqdiss:27670088

Felfelani, F., Pokhrel, Y., Guan, K., & Lawrence, D. M. (2018). Utilizing SMAP soil moisture data to constrain irrigation in the Community Land Model. *Geophysical Research Letters*, *45*(23), 12892–12902. https://doi.org/10.1029/2018GL080870

Felfelani, F., Wada, Y., Longuevergne, L., & Pokhrel, Y. (2017). Natural and human-induced terrestrial water storage change: A global analysis using hydrological models and GRACE. *Journal of Hydrology*, *553*, 105–118. https://doi.org/10.1016/j.jhydrol.2017.07.048

Gleeson, T., Marklund, L., Smith, L., & Manning, A. H. (2011). Classifying the water table at regional to continental scales. *Geophysical Research Letters*, *38*(5), L05401. https://doi.org/10.1029/2010GL046427

Gleeson, T., Moosdorf, N., Hartmann, J., & van Beek, L. P. H. (2014). A glimpse beneath earth's surface: GLobal HYdrogeology MaPS (GLHYMPS) of permeability and porosity. *Geophysical Research Letters*, *41*(11), 3891–3898. https://doi.org/10.1002/2014GL059856

Gleeson, T., Wada, Y., Bierkens, M. F. P., & van Beek, L. P. H. (2012). Water balance of global aquifers revealed by groundwater footprint. *Nature*, *488*(7410), 197–200. https://doi.org/10.1038/nature11295

Gouriéroux, C., Holly, A., & Monfort, A. (1982). Likelihood ratio test, Wald test, and Kuhn-Tucker test in linear models with inequality constraints on the regression parameters. *Econometrica*, *50*(1), 63–80. https://doi.org/10.2307/1912529

Huscroft, J., Gleeson, T., Hartmann, J., & Börker, J. (2018). Compiling and mapping global permeability of the unconsolidated and consolidated earth: GLobal HYdrogeology MaPS 2.0 (GLHYMPS 2.0). *Geophysical Research Letters*, *45*(4), 1897–1904. https://doi.org/10.1002/2017GL075860

Kendall, M. G. (1975). *Rank correlation methods*. London, UK: Griffin.

Koirala, S., Kim, H., Hirabayashi, Y., Kanae, S., & Oki, T. (2019). Sensitivity of global hydrological simulations to groundwater capillary flux parameterizations. *Water Resources Research*, *55*(1), 402–425. https://doi.org/10.1029/2018WR023434

Kollet, S. J., & Maxwell, R. M. (2008). Capturing the influence of groundwater dynamics on land surface processes using an integrated, distributed watershed model. *Water Resources Research*, *44*(2), W02402. https://doi.org/10.1029/2007WR006004

Krakauer, N. Y., Li, H., & Fan, Y. (2014). Groundwater flow across spatial scales: Importance for climate modeling. *Environmental Research Letters*, *9*(3), 034003. https://doi.org/10.1088/1748-9326/9/3/034003

Lawrence, D. M., Fisher, R. A., Koven, C. D., Oleson, K. W., Swenson, S. C., Bonan, G., et al. (2019). The Community Land Model version 5: Description of new features, benchmarking, and impact of forcing uncertainty. *Journal of Advances in Modeling Earth Systems*, *11*(12), 4245–4287. https://doi.org/10.1029/2018MS001583

Lawrence, D. M., Oleson, K. W., Flanner, M. G., Thornton, P. E., Swenson, S. C., Lawrence, P. J., et al. (2011). Parameterization improvements and functional and structural advances in version 4 of the Community Land Model. *Journal of Advances in Modeling Earth Systems*, *3*(1), M03001. https://doi.org/10.1029/2011MS00045

Leng, G., Huang, M., Tang, Q., Gao, H., & Leung, L. R. (2014). Modeling the effects of groundwater-fed irrigation on terrestrial hydrology over the conterminous United States. *Journal of Hydrometeorology*, *15*(3), 957–972. https://doi.org/10.1175/JHM-D-13-049.1

Leng, G., Huang, M., Tang, Q., Sacks, W. J., Lei, H., & Leung, L. R. (2013). Modeling the effects of irrigation on land surface fluxes and states over the conterminous United States: Sensitivity to input data and model parameters. *Journal of Geophysical Research: Atmospheres*, *118*(17), 9789–9803. Retrieved from https://agupubs.onlinelibrary.wiley.com/doi/full/10.1002/jgrd.50792

Liang, X., Xie, Z., & Huang, M. (2003). A new parameterization for surface and groundwater interactions and its impact on water budgets with the variable infiltration capacity (VIC) land surface model. *Journal of Geophysical Research*, *108*(D16), 8613. https://doi.org/10.1029/2002JD003090

Li, H., Wigmosta, M. S., Wu, H., Huang, M., Ke, Y., Coleman, A. M., & Leung, L. R. (2013). A physically based runoff routing model for land surface and earth system models. *Journal of Hydrometeorology*, *14*(3), 808–828. https://doi.org/10.1175/JHM-D-12-015.1

Long, D., Longuevergne, L., & Scanlon, B. R. (2015). Global analysis of approaches for deriving total water storage changes from GRACE satellites. *Water Resources Research*, *51*(4), 2574–2594. https://doi.org/10.1002/2014WR016853

Longuevergne, L., Scanlon, B. R., & Wilson, C. R. (2010). GRACE Hydrological estimates for small basins: Evaluating processing approaches on the High Plains Aquifer, USA. *Water Resources Research*, *46*(11), W11517. https://doi.org/10.1029/2009WR008564

Mann, H. B. (1945). Nonparametric tests against trend. *Econometrica*, *13*(3), 245–259. https://doi.org/10.2307/1907187

Maupin, M. A., Kenny, J. F., Hutson, S. S., Lovelace, J. K., Barber, N. L., & Linsey, K. S. (2014). *Estimated use of water in the United States in 2010* (USGS Circular 1405, p. 56). Reston, VA: US Geological Survey. https://doi.org/10.3133/cir1405

Maxwell, R. M., & Condon, L. E. (2016). Connections between groundwater flow and transpiration partitioning. *Science*, *353*(6297), 377–380. https://doi.org/10.1126/science.aaf7891

Maxwell, R. M., & Miller, N. L. (2005). Development of a coupled land surface and groundwater model. *Journal of Hydrometeorology*, *6*(3), 233–247. https://doi.org/10.1175/JHM422.1

McGuire, V. L. (2011). *Water-level changes in the High Plains Aquifer, predevelopment to 2009, 2007–08, and 2008–09, and change in water in storage, predevelopment to 2009*, Reston, VA: Publications of the US Geological Survey. Retrieved from https://digitalcommons.unl.edu/usgspubs/105

McGuire, V. L. (2014). *Water-level changes and change in water in storage in the High Plains Aquifer, predevelopment to 2013 and 2011–13* (USGS Numbered Series No. 2014–5218). Reston, VA: US Geological Survey. Retrieved from https://pubs.usgs.gov/sir/2014/5218/

McGuire, V. L. (2017). *Water-level and recoverable water in storage changes, High Plains aquifer, predevelopment to 2015 and 2013–15* (USGS Numbered Series No. 2017–5040). Reston, VA: US Geological Survey. Retrieved from http://pubs.er.usgs.gov/publication/sir20175040

Miguez-Macho, G., Fan, Y., Weaver, C. P., Walko, R., & Robock, A. (2007). Incorporating water table dynamics in climate modeling: 2. Formulation, validation, and soil moisture simulation. *Journal of Geophysical Research*, *112*, D13108. https://doi.org/10.1029/2006JD008112

Nie, W., Zaitchik, B. F., Rodell, M., Kumar, S. V., Anderson, M. C., & Hain, C. (2018). Groundwater withdrawals under drought: Reconciling GRACE and land surface models in the United States High Plains Aquifer. *Water Resources Research*, *54*(8), 5282–5299. https://doi.org/10.1029/2017WR022178

Nie, W., Zaitchik, B. F., Rodell, M., Kumar, S. V., Arsenault, K. R., Li, B., & Getirana, A. (2019). Assimilating GRACE into a land surface model in the presence of an irrigation-induced groundwater trend. *Water Resources Research*, *55*(12), 11274–11294. https://doi.org/10.1029/2019WR025363

Niu, G.-Y., Yang, Z.-L., Dickinson, R. E., & Gulden, L. E. (2005). A simple TOPMODEL-based runoff parameterization (SIMTOP) for use in global climate models. *Journal of Geophysical Research*, *110*(D21), D21106. https://doi.org/10.1029/2005JD006111

Niu, G.-Y., Yang, Z.-L., Mitchell, K. E., Chen, F., Ek, M. B., Barlage, M., et al. (2011). The community Noah land surface model with multiparameterization options (Noah-MP): 1. Model description and evaluation with local-scale measurements. *Journal of Geophysical Research*, *116*(D12), D12109. https://doi.org/10.1029/2010JD015139

Oleson, K., Lawrence, D. M., Bonan, G. B., Drewniak, B., Huang, M., Koven, C. D., et al. (2013). *Technical description of version 4.5 of the Community Land Model (CLM)* (NCAR Technical Note NCAR/TN-503+STR, p. 420). Boulder, CO. https://doi.org/10.5065/D6RR1W7M

Panday, S., Langevin, C. D., Niswonger, R. G., Ibaraki, M., & Hughes, J. D. (2013). *MODFLOW–USG version 1: An unstructured grid version of MODFLOW for simulating groundwater flow and tightly coupled processes using a control volume finite-difference formulation* (Techniques and Methods 6-A45, p. 66). Reston, VA: US Geological Survey. Retrieved from https://pubs.usgs.gov/tm/06/a45

Pelletier, J. D., Broxton, P. D., Hazenberg, P., Zeng, X., Troch, P. A., Niu, G.-Y., et al. (2016). A gridded global data set of soil, intact regolith, and sedimentary deposit thicknesses for regional and global land surface modeling. *Journal of Advances in Modeling Earth Systems*, *8*(1), 41–65. https://doi.org/10.1002/2015MS000526

Pokhrel, Y., Fan, Y., Miguez-Macho, G., Yeh, P. J.-F., & Han, S.-C. (2013). The role of groundwater in the Amazon water cycle: 3. Influence on terrestrial water storage computations and comparison with GRACE. *Journal of Geophysical Research: Atmospheres*, *118*(8), 3233–3244. https://doi.org/10.1002/jgrd.50335

Pokhrel, Y., Felfelani, F., Shin, S., Yamada, T. J., & Satoh, Y. (2017). Modeling large-scale human alteration of land surface hydrology and climate. *Geoscience Letters*, *4*(1), 10. https://doi.org/10.1186/s40562-017-0076-5

Pokhrel, Y., Hanasaki, N., Koirala, S., Cho, J., Yeh, P. J.-F., Kim, H., et al. (2012). Incorporating anthropogenic water regulation modules into a land surface model. *Journal of Hydrometeorology*, *13*(1), 255–269. https://doi.org/10.1175/JHM-D-11-013.1

Pokhrel, Y., Hanasaki, N., Wada, Y., & Kim, H. (2016). Recent progresses in incorporating human land–water management into global land surface models toward their integration into Earth system models. *Wiley Interdisciplinary Reviews: Water*, *3*(4), 548–574. https://doi.org/10.1002/wat2.1150

Pokhrel, Y., Koirala, S., Yeh, P. J.-F., Hanasaki, N., Longuevergne, L., Kanae, S., & Oki, T. (2015). Incorporation of groundwater pumping in a global land surface model with the representation of human impacts. *Water Resources Research*, *51*(1), 78–96. https://doi.org/10.1002/2014WR015602

Raiber, M., Lewis, S., Cendón, D. I., Cui, T., Cox, M. E., Gilfedder, M., & Rassam, D. W. (2019). Significance of the connection between bedrock, alluvium and streams: A spatial and temporal hydrogeological and hydrogeochemical assessment from queensland, Australia. *Journal of Hydrology*, *569*, 666–684. https://doi.org/10.1016/j.jhydrol.2018.12.020

Richards, L. A. (1931). Capillary conduction of liquids through porous mediums. *Journal of Applied Physics*, *1*(5), 318–333. https://doi.org/10.1063/1.1745010

Rodell, M., Famiglietti, J. S., Wiese, D. N., Reager, J. T., Beaudoing, H. K., Landerer, F. W., & Lo, M.-H. (2018). Emerging trends in global freshwater availability. *Nature*, *557*, 651–659. https://doi.org/10.1038/s41586-018-0123-1

Rodell, M., Velicogna, I., & Famiglietti, J. S. (2009). Satellite-based estimates of groundwater depletion in India. *Nature*, *460*(7258), 999–1002. https://doi.org/10.1038/nature08238

Save, H., Bettadpur, S., & Tapley, B. D. (2016). High-resolution CSR GRACE RL05 mascons. *Journal of Geophysical Research: Solid Earth*, *121*(10), 7547–7569. https://doi.org/10.1002/2016JB013007

Scanlon, B. R., Faunt, C. C., Longuevergne, L., Reedy, R. C., Alley, W. M., McGuire, V. L., & McMahon, P. B. (2012). Groundwater depletion and sustainability of irrigation in the US High Plains and Central Valley. *Proceedings of the National Academy of Sciences of the United States of America*, *109*(24), 9320–9325 https://doi.org/10.1073/pnas.1200311109

Scanlon, B. R., Longuevergne, L., & Long, D. (2012). Ground referencing GRACE satellite estimates of groundwater storage changes in the California Central Valley, USA. *Water Resources Research*, *48*(4), W04520. https://doi.org/10.1029/2011WR011312

Scanlon, B. R., Zhang, Z., Save, H., Wiese, D. N., Landerer, F. W., Long, D., et al. (2016). Global evaluation of new GRACE mascon products for hydrologic applications. *Water Resources Research*, *52*(12), 9412–9429. https://doi.org/10.1002/2016WR019494

Shin, S., Pokhrel, Y., & Miguez-Macho, G. (2019). High-resolution modeling of reservoir release and storage dynamics at the continental scale. *Water Resources Research*, *55*(1), 787–810. https://doi.org/10.1029/2018WR023025

Siebert, S., Burke, J., Faures, J. M., Frenken, K., Hoogeveen, J., Döll, P., & Portmann, F. T. (2010). Groundwater use for irrigation—A global inventory. *Hydrology and Earth System Sciences*, *14*(10), 1863–1880. https://doi.org/10.5194/hess-14-1863-2010

Sophocleous, M. (2002). Interactions between groundwater and surface water: The state of the science. *Hydrogeology Journal*, *10*(1), 52–67. https://doi.org/10.1007/s10040-001-0170-8

Swenson, S. C., Clark, M., Fan, Y., Lawrence, D. M., & Perket, J. (2019). Representing intrahillslope lateral subsurface flow in the Community Land Model. *Journal of Advances in Modeling Earth Systems*, *11*(12), 4044–4065. https://doi.org/10.1029/2019MS001833

Swenson, S. C., & Lawrence, D. M. (2015). A GRACE-based assessment of interannual groundwater dynamics in the Community Land Model. *Water Resources Research*, *51*(11), 8817–8833. https://doi.org/10.1002/2015WR017582

Wada, Y., Bierkens, M. F. P., de Roo, A., Dirmeyer, P. A., Famiglietti, J. S., Hanasaki, N., et al. (2017). Human–water interface in hydrological modelling: Current status and future directions. *Hydrology and Earth System Sciences*, *21*(8), 4169–4193. https://doi.org/10.5194/hess-21-4169-2017

Wada, Y., van Beek, L. P. H., van Kempen, C. M., Reckman, J. W. T. M., Vasak, S., & Bierkens, M. F. P. (2010). Global depletion of groundwater resources. *Geophysical Research Letters*, *37*(20), L20402. https://doi.org/10.1029/2010GL044571

Wada, Y., Wisser, D., & Bierkens, M. F. P. (2014). Global modeling of withdrawal, allocation and consumptive use of surface water and groundwater resources. *Earth System Dynamics*, *5*(1), 15–40. https://doi.org/10.5194/esd-5-15-2014

Wahr, J., Molenaar, M., & Bryan, F. (1998). Time variability of the Earth's gravity field: Hydrological and oceanic effects and their possible detection using GRACE. *Journal of Geophysical Research*, *103*(B12), 30205–30229. https://doi.org/10.1029/98JB02844

Watkins, M. M., Wiese, D. N., Yuan, D.-N., Boening, C., & Landerer, F. W. (2015). Improved methods for observing Earth's time variable mass distribution with GRACE using spherical cap mascons. *Journal of Geophysical Research: Solid Earth*, *120*(4), 2014JB011547. 2648–2671. https://doi.org/10.1002/2014JB011547

Wiese, D. N., Landerer, F. W., & Watkins, M. M. (2016). Quantifying and reducing leakage errors in the JPL RL05M GRACE mascon solution: GRACE JPL RL05M leakage error reduction. *Water Resources Research*, *52*(9), 7490–7502. https://doi.org/10.1002/2016WR019344

Wiese, D. N., Yuan, D.-N., Boening, C., Landerer, F. W., & Watkins, M. M. (2016). *JPL GRACE mascon ocean, ice, and hydrology equivalent water height RL05M.1 CRI filtered version 2*. Pasadena, CA: PO.DAAC. https://doi.org/10.5067/TEMSC-2LCR5

Williamson, A. K., Prudic, D. E., & Swain, L. A. (1989). *Ground-water flow in the Central Valley, California* (USGS Professional Paper 1401-D). Washington, DC: United States Geological Survey. Retrieved from https://www.osti.gov/biblio/6265446

Winter, T. C., Harvey, J. W., Franke, O. L., & Alley, W. M. (1998). *Ground water and surface water: A single resource* (USGS Circular 1139). Denver, CO: US Geological Survey.

Xie, Z., Liu, S., Zeng, Y., Gao, J., Qin, P., Jia, B., et al. (2018). A high-resolution land model with groundwater lateral flow, water use, and soil freeze-thaw front dynamics and its applications in an endorheic basin. *Journal of Geophysical Research: Atmospheres*, *123*(14), 7204–7222. https://doi.org/10.1029/2018JD028369

Yamada, T. J., & Pokhrel, Y. (2019). Effect of human-induced land disturbance on subseasonal predictability of near-surface variables using an atmospheric general circulation model. *Atmosphere*, *10*(11), 725. https://doi.org/10.3390/atmos10110725

Yokohata, T., Kinoshita, T., Sakurai, G., Pokhrel, Y., Ito, A., Okada, M., et al. (2020). MIROC-INTEG-LAND version 1: a global biogeochemical land surface model with human water management, crop growth, and land-use change. *Geoscientific Model Development*, *13*(10), 4713–4747. https://doi.org/10.5194/gmd-13-4713-2020

Zeng, Y., Xie, Z., Liu, S., Xie, J., Jia, B., Qin, P., & Gao, J. (2018). Global land surface modeling including lateral groundwater flow. *Journal of Advances in Modeling Earth Systems*, *10*(8), 1882–1900. https://doi.org/10.1029/2018MS001304

Zeng, Y., Xie, Z., Yu, Y., Liu, S., Wang, L., Zou, J., et al. (2016). Effects of anthropogenic water regulation and groundwater lateral flow on land processes. *Journal of Advances in Modeling Earth Systems*, *8*(3), 1106–1131. https://doi.org/10.1002/2016MS000646